Miner Deposita (2007) 42:65–87
DOI 10.1007/s00126-006-0096-0

ARTICLE

The role of decarbonization and structure in the Callie gold deposit, Tanami Region of northern Australia

Nicholas C. Williams

Received: 11 April 2005 / Accepted: 16 August 2006 / Published online: 3 October 2006
© Springer-Verlag 2006

Abstract The Callie deposit is the largest (6.0 Moz Au) of several gold deposits in the Dead Bullock Soak goldfield of the Northern Territory's Tanami Region, 550 km northwest of Alice Springs. The Callie ore lies within corridors, up to 180 m wide, of sheeted en echelon quartz veins where they intersect the 500-m-wide hinge of an ESE-plunging F_1 anticlinorium. The host rocks are the Blake beds, of the Paleoproterozoic Dead Bullock Formation, which consist of a >350-m-thick sequence of lower greenschist facies graphitic turbidites and mudstones overlying in excess of 100 m of thickly bedded siltstones and fine sandstones. The rocks are Fe-rich and dominated by assemblages of chlorite and biotite, both of which are of hydrothermal and metamorphic origin. A fundamental characteristic of the hydrothermal alteration is the removal of graphite, a process which is associated with bleaching and the development of bedding-parallel bands of coarse biotite augen. Gold is found only in quartz veins and only where they cut decarbonized chloritic rock with abundant biotite augen and no sulfide minerals. Auriferous quartz veins differ from barren quartz veins by the presence of ilmenite, apatite, xenotime, and gold and the absence of sulfide minerals. The assemblage of gold–ilmenite–apatite–xenotime indicates a linked genesis and mobility of Ti, P, and Y in the mineralizing fluids. Geochemical analysis of samples throughout the deposit shows that gold only occurs in sedimentary rocks with high $FeO/(FeO+Fe_2O_3)$ and low $C/(C+CO_2)$ ratios (>0.8 and <0.2, respectively). This association can be explained by reactions that convert C from reduced graphitic host rocks into CO_2 and reduce ferric iron in the host rocks to ferrous iron in biotite and chlorite. These reactions would increase the CO_2 content of the fluid, facilitating the transport of Ti, P, and Y from the host rocks into the veins. Both CO_2 and CH_4 produced by reaction of H_2O with graphite, effervesced under the lower confining pressures in the veins. This would have partitioned H_2S into the vapor phase, destabilizing Au–bisulfide complexes; the loss of CO_2 and H_2S from the aqueous phase caused precipitation of gold, ilmenite, apatite, and xenotime. It is proposed that this process was the main control on gold precipitation. Oxidization of iron in the very reduced wall rocks, resulting in reduction of the fluid, provided a second mechanism of gold precipitation in previously decarbonized rocks, contributing to the high grades in some samples. Although sulfide minerals, especially arsenopyrite, did form during the hydrothermal event, host rock sulfidation reactions did not play a role in gold precipitation because gold is absent near rocks or veins containing sulfide minerals. Sulfide minerals likely formed by different mechanisms from those associated with gold deposition. Both the fold architecture and subsequent spatially coincident sinistral semibrittle shearing ensured that the ore fluids were strongly focused into the hinges of the anticlines. Within the anticlines, a reactive cap of fine-grained, graphitic, reduced Fe-rich turbidites above more permeable siltstones and fine sandstones impeded fluid flow ensuring efficient removal of graphite, and the associated effervescence of CO_2 from the fluid caused the

Editorial handling: D. Huston

N. C. Williams
Geoscience Australia, GPO Box 378, Canberra,
Australian Capital Territory, 2601, Australia

Present address:
N. C. Williams (✉)
Mineral Deposit Research Unit, Department of Earth and Ocean Sciences, The University of British Columbia,
6339 Stores Road, Vancouver,
British Columbia, V6T 1Z4, Canada
e-mail: nwilliams@eos.ubc.ca

precipitation of gold. Exploration for similar deposits should focus on the intersection of east–west shear zones with folds and Fe-rich graphitic host rocks.

Keywords Gold deposits · Tanami Region · Quartz veins · Graphite · Geochemistry

Introduction

Callie is one of the several gold deposits located in the Dead Bullock Soak (DBS) goldfield in the Tanami Region of Australia's Northern Territory (Fig. 1), 550 km northwest of Alice Springs. The deformed and metamorphosed Archean and Paleoproterozoic rocks of the region host a number of other gold deposits, including The Granites, 40 km east of DBS (Mayer 1990), a corridor of deposits at Tanami (Tunks and Marsh 1998), and the Groundrush deposit, 100 km north of The Granites (Huston et al. 2006). The deposits vary in size and mineralization style and are hosted in a variety of rock types, including dolerite, banded iron formations (BIFs), and metasedimentary rocks. Callie is by far the largest deposit in the region, with coarse gold (from <1 mm to several centimeters in diameter) hosted by thin, sheeted quartz veins within lower greenschist facies sedimentary rocks that are folded into a 3-km-wavelength east–southeast-trending anticlinorium. The host anticlinorium is delineated by a discrete east–southeast-oriented aeromagnetic high that is <2 km wide and >45 km long. Gold was discovered at DBS in 1988 in a BIF, and gold was first found at Callie in October 1991 (Smith et al. 1998). Exploration and mining are presently being carried out at DBS by Newmont Mining Corporation (formerly Normandy NFM). The Callie deposit was initially mined as an open cut but is now an underground operation. It has past production of 10.0 Mt at 5.1 g/t Au and a present resource of 22.0 Mt at 6.1 g/t Au with the ore body remaining open at depth (Huston et al. 2006).

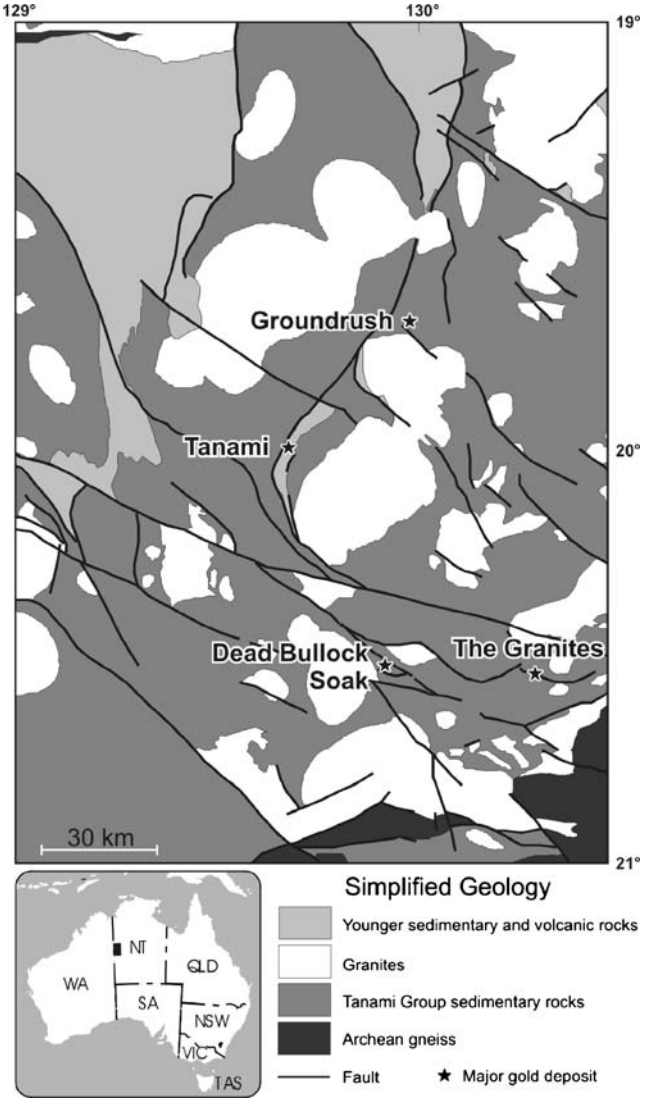

Fig. 1 Location map showing the position of Dead Bullock Soak (including Callie), The Granites, Groundrush, and the Tanami goldfields within the Northern Territory with respect to sedimentary sequences and intrusions. Modified from Huston et al. (2006)

The relatively large tonnage and consistent grade of the Callie deposit and the continuing exploration and development of the Tanami Region despite its remote location and high proportion of cover have highlighted the need to improve the current understanding of mineralizing processes in the district. Several possible features conducive to lode gold formation have previously been proposed by Smith et al. (1998) and Hendrickx et al. (2000), including faulting, folding, and passive lithological controls; this study was specifically aimed at identifying the relative contributions of each to the development of the large gold deposit at Callie. The study also aims to supplement the existing knowledge of the geology and stratigraphy (Voulgaris and Emslie 2004) with a more detailed analysis of the petrography, geochemistry, and structure associated with mineralization.

Materials and methods

During this study, drill core logging, pit mapping, and limited underground structural work were undertaken at the Callie mine. Five diamond drill holes were logged in detail on north–south sections 596000 and 602000 mE (UTM Map Grid of Australia zone 52) through the ore zone. A total of 335 samples were collected as two batches. The first batch consisted of 147 split pulp samples taken at 5-m intervals (with several gaps) from Normandy NFM's 1-m-long assay intervals on holes DBD395, DBD395D2, DBD395D4, and DBD395D5 in the 602000 mE section.

The second batch of 188 samples was selected from diamond drill core (holes DBD364 and DBD415 from section 596000 mE and holes DBD395, DBD395D3, and DBD395D5 from section 602000 mE) logged during fieldwork. A limited number of measurements were made in the field with a GMS-2 hand-held magnetic susceptibility meter on half-core samples.

Polished thin sections were made from 16 core samples, and covered thin sections were made from another 13 core samples. Microprobe analyses were obtained on the polished thin sections using an EDS-WDS-equipped Camebax microprobe at the Research School of Earth Sciences, Australian National University. Mineral identification of some phases was further assisted on polished thin sections by the use of a Dilor SuperLabram confocal Raman microprobe at Geoscience Australia.

Whole rock major and trace element analyses were performed on 228 samples. All of the first batch of 147 split pulp samples were analyzed. A second batch of 81 samples with minimal veining was selected from the drill core samples collected during fieldwork. Samples in both batches were prepared using a steel crusher and a tungsten-carbide mill, the first batch by Normandy NFM and the second batch at Geoscience Australia. Major, minor, and trace element geochemical analyses (except Au) were performed at Geoscience Australia's geochemical laboratory using either a Perkin Elmer Elan 6000 ICP-MS and the methods of Jenner et al. (1990) and Pyke (2000), or a Philips PW2404 4 kW sequential X-ray fluorescence (XRF) spectrometer following Norrish and Chappell (1977). The concentrations of FeO were measured by titrimetry on a Metrohm 716 DMS Titrino using a modification of the technique of Shapiro and Brannock (1962). In this text, $Fe_2O_3^T$ or FeO^T represents (in weight percent) the total iron content expressed as Fe_2O_3 or FeO, respectively, whereas references to Fe_2O_3 or FeO represent their actual content. All samples were analyzed for carbonate carbon (CO_2; following total digestion by HF and HNO_3) and organic carbon (C; following digestion by HCl) on a LECO RC412 analyzer. Gold assays were performed on 1-m intervals by fire assay for Normandy NFM by Analabs.

Twenty powder splits from the second batch of samples were analyzed by X-ray diffraction (XRD) at Geoscience Australia using a Siemens D500/501 Diffractometer with 2θ measurements taken in the interval from 2 to 62°. Organic concentrates were made from 26 samples by repeated leaching with HF and BF_3 acids (after Robl and Davis 1993) before carbon isotope analysis of the organic carbon component. Of these, 11 concentrates had enough carbon for analysis on a Finnigan MAT 252 mass spectrometer coupled to a Carlo Erba elemental analyzer. The resulting $\delta^{13}C$ data are reported in per mil (‰) notation relative to the PDB standard.

Regional geology

Stratigraphy

Hendrickx et al. (2000), Vandenberg et al. (2001), and Dean (2001) have described the geology, stratigraphy, igneous rocks, and structure of the Tanami Region in detail. A brief summary of their findings is included in this study. The basement rocks in the region are inferred to be banded granitic gneisses of the Archean Billabong Complex (Cooper and Ding 1997), but they have not been observed near DBS. The DBS deposits are completely hosted within fine-grained metasedimentary rocks of the Dead Bullock Formation (which includes carbonaceous mudstone, siltstone, chert, and BIF), the lower unit in the Paleoproterozoic Tanami Group. The Dead Bullock Formation represents a quiet marine depositional environment on a passive margin, similar to other Tanami Group rocks. It was intruded by 1,840–1,800 Ma granites (Hendrickx et al. 2000) and faulted into contact with the Archean basement rocks. Cross and Crispe (2006) report an age of 1,838±6 Ma for the Dead Bullock Formation based on a tuff from the upper part of the unit. The Killi Killi Formation, a thick monotonous package of turbiditic metasandstone, forms the upper unit of the Tanami Group, overlying the Dead Bullock Formation. The Killi Killi Formation represents the last episode of sedimentation before the Tanami orogenic event at ~1835–1825 Ma (Crispe et al. 2006). Several granite suites and numerous dolerite sills intruded the Tanami Group. Their ages are poorly constrained, but most are foliated and are inferred to predate major deformation.

The Tanami Group is unconformably overlain by sedimentary and volcanic rocks of the Ware Group, which was deposited at 1825–1815 Ma (Cross and Crispe 2006). The relative and absolute age of the Mount Charles Formation, which hosts the Tanami goldfield, is unclear at present. The Pargee Sandstone, a thick sequence of shallow, marine, siliciclastic, sedimentary rocks, which includes conglomerate, quartz arenite, and siltstone, unconformably overlies the Ware Group. Detrital zircons within the Pargee Sandstone give a maximum depositional age of about 1,760 Ma (Cross and Crispe 2006).

Structure

Smith et al. (1998) and Vandenberg et al. (2001) have described the structural geology of DBS goldfield and the Tanami Region, a summary of which is presented in this study. Greenschist to amphibolite facies metamorphism and formation of the dominant east–southeast-plunging F_1 folds at DBS, including the DBS anticlinorium (Figs. 2 and 3), were associated with M_1 and D_1, respectively, and likely occurred during the Tanami orogenic event. Continued

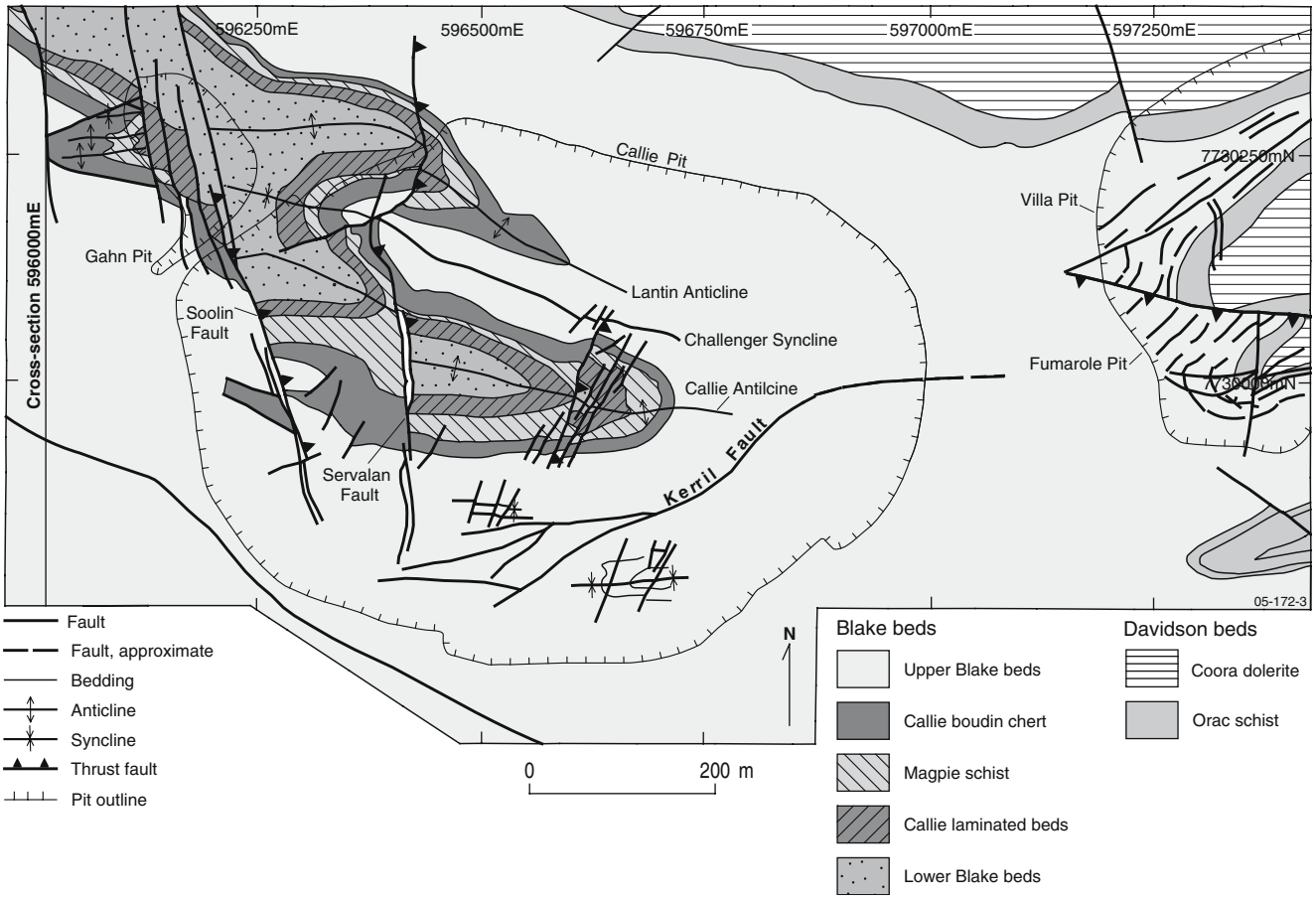

Fig. 2 Simplified near-surface geological plan of the Callie deposit (1,380 m level). All units shown belong to the Dead Bullock Formation. Position of the cross section in Fig. 3 is also shown. Modified from Wygralak et al. (2001)

deformation during that event formed D_2 east–southeast plunging interference folds (F_2) at a slight angle to the main F_1 folds at DBS. Minor west–southwest plunging F_3 folds formed at DBS during D_3. Extension and granite intrusion occurred regionally during D_4 but more strongly affected higher stratigraphic levels and are not clearly recognized at DBS. Thrust faulting, shearing, and oblique-slip faulting during D_5 are coincident with gold mineralization at DBS. Late D_{6+} faulting, including movement on thrust, oblique-slip, and normal faults, offsets all earlier structures. At DBS, D_{6+} structures include the east-trending Kerril Fault, the south-trending Soolin Fault, and the south-trending, east-dipping Servalan Fault, which all offset the ore and stratigraphy (Fig. 2). The timing relationships among these late structures are unclear, although the Kerril Fault postdates mineralization and is truncated by both the Soolin and Servalan Faults.

Local geology

The Dead Bullock Formation in the DBS goldfield has been subdivided into a number of informal names. The lowermost package, which is termed the Blake beds (Fig. 4), comprises siltstone and thin turbidite deposits, whereas the upper package, which is termed the Davidson beds, comprises siltstone and iron-rich rocks (locally termed "iron formation"). The Blake beds were the only rocks observed in this study; in general, they are too fine-grained and too altered and metamorphosed to reliably identify the original mineralogy. The analysis by XRD and the petrographic study of least altered samples in different units suggest that the most common components of the original detrital mineralogy of all the rocks in the Blake beds were varying proportions of graphite, quartz, albite, and ilmenite or rutile. Large hydrothermal arsenopyrite crystals trap many small mineral inclusions, typically including orthoclase, albite, chlorite, apatite, and calcite, and these may also represent early constituents of the rocks. Some muscovite, biotite, and chlorite may have been detrital or diagenetic in origin, but all of these minerals were also pervasively introduced during metamorphism or alteration.

Smith et al. (1998) first described the informal subdivisions of the Dead Bullock Formation used in this study, and further descriptions are provided by Voulgaris and Emslie (2004). Although all units have undergone greens-

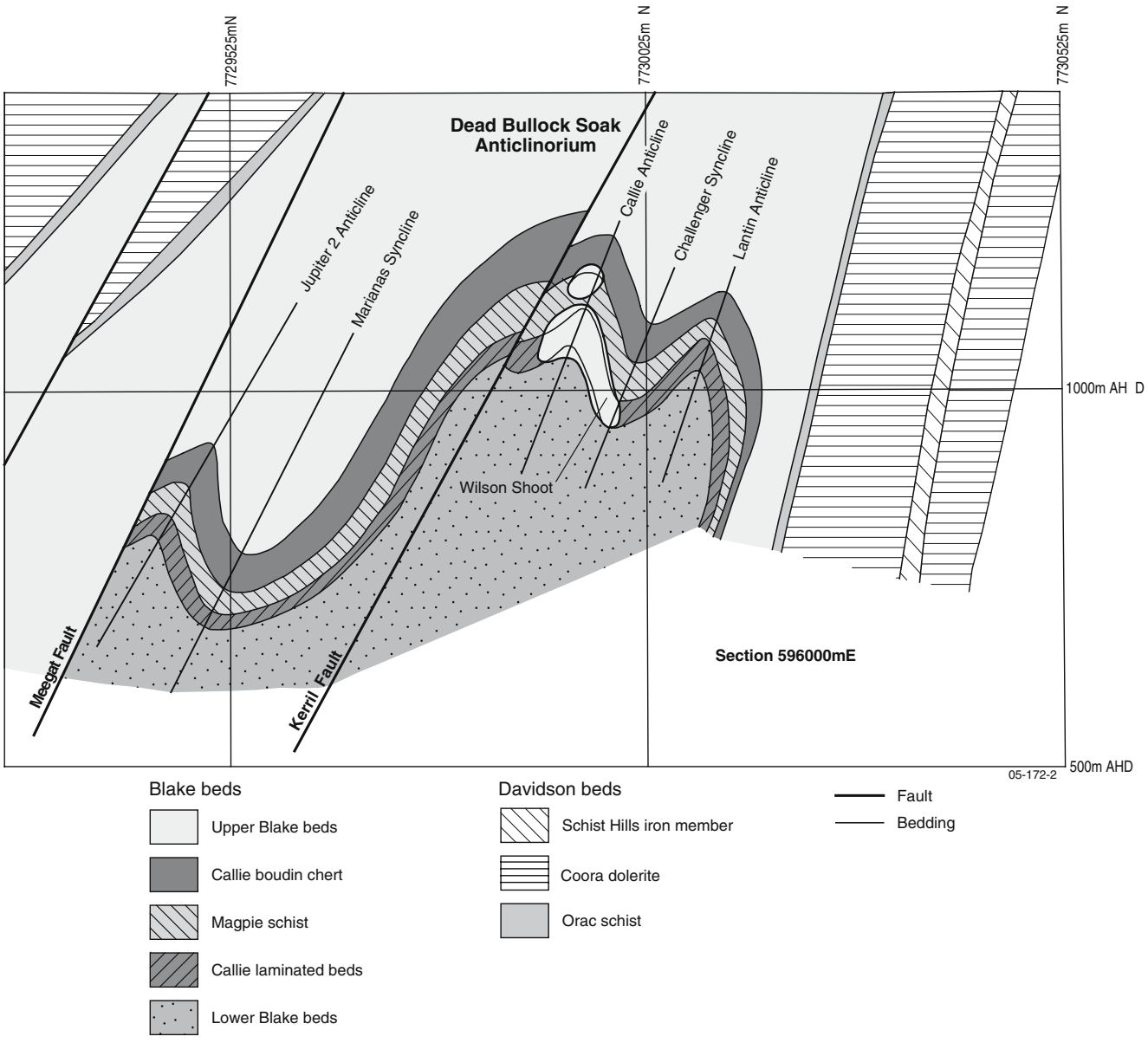

Fig. 3 Schematic south–north cross section (596000 mE; UTM Map Grid of Australia zone 52 coordinates) showing the DBS anticlinorium, Kerril Fault, and the Wilson Shoot ore zone. Wilson Shoot is the initial discovery ore zone within the main quartz vein corridor (QVC) and was mined from the open pit. Underground mining has followed the QVC east, across Challenger Syncline, into the Lantin Anticline. All units shown belong to the Dead Bullock Formation. Modified from D. Larsen, written communication 2001

chist facies metamorphism, they are described by their protoliths which are clearly recognizable. The Lower Blake beds are the oldest unit of the Blake beds and consist of massive, nongraphitic coarse-grained siltstone and fine-grained sandstone that lack graphite even in least-altered examples. The upper part of the Lower Blake beds contains a 3- to 20-m-thick interval of nongraphitic fine-grained turbidite deposits, locally known as the Lower Blake laminations. Both the Lower Blake beds and the Lower Blake laminations contain zones rich in magnetite. Although the thickness of the Lower Blake beds is unknown, it is more than a few hundred meters.

These lower units are conformably overlain by the ~15-m-thick Callie laminated beds (the Callie host unit of Smith et al. 1998), which consist of 6- to 9-cm-thick turbidites. The Callie laminated beds grade upward into rocks of the Magpie schist. The Magpie schist is about 40 m thick and contains beds of variable thickness, commonly <1 cm but occasionally up to 30–40 cm thick, of graphitic mudstones interbedded with nongraphitic siltstone. The Magpie schist grades up into the 20-m-thick Callie boudin chert that provides the only marker unit in the sequence with its distinctive egg-shaped cherty boudins, as much as 3–5 cm in diameter, hosted in graphitic fine-grained mudstones

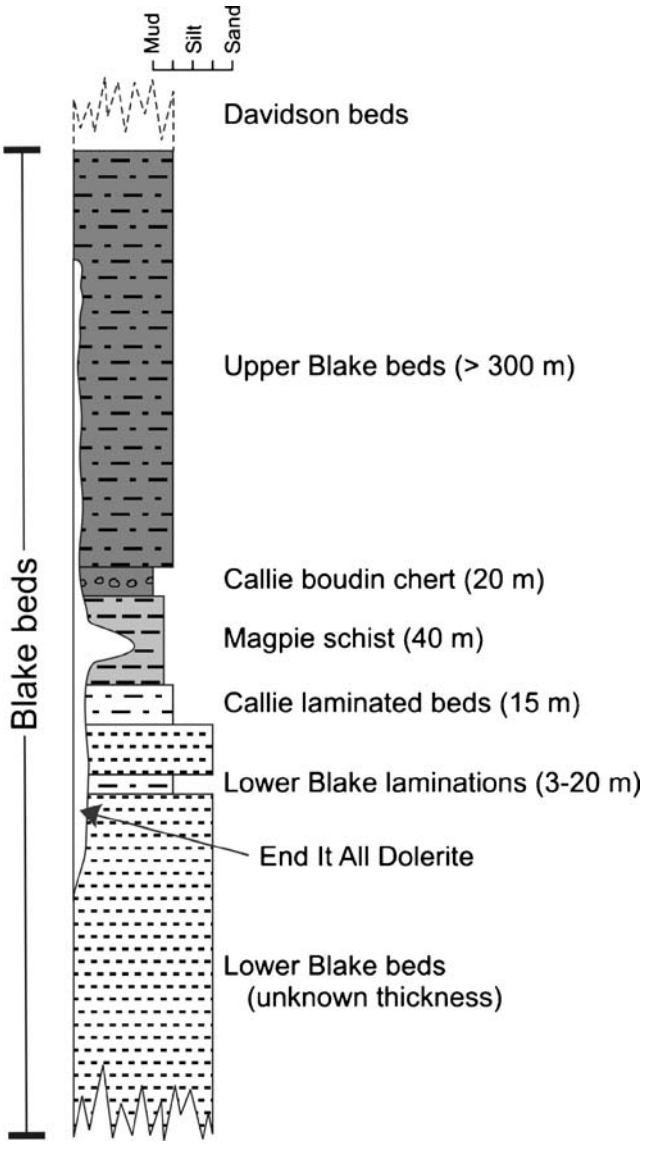

Fig. 4 Stratigraphic column of the Blake beds, the oldest member of the Dead Bullock Formation, at Callie, approximately to scale. All units shown belong to the Dead Bullock Formation. The *column width* reflects average grain size, and the *shading* indicates relative current abundance of graphite, with *darker colors* indicating more graphite. The units with the smallest grain sizes, the Callie boudin chert and Magpie schist as well as the lower portions of the Upper Blake beds, commonly show partial decarbonization textures above the ore zones, which are typically hosted by the decarbonized Callie laminated beds and Lower Blake laminations

several centimeters thick. Overall, there is a fining-upward sequence from the nongraphitic siltstones and fine sandstones of the Lower Blake beds up to the graphitic mudstone and siltstone of the Magpie schist and the Callie boudin chert mudstones (Fig. 4). The Callie boudin chert grades up into the Upper Blake beds, which extend for >300 m up to the base of the Davidson beds. The Upper Blake beds are generally thin (<1 cm), graphitic, rhythmic, graded turbidite beds, with local interbeds of thicker mudstone and siltstone.

Several generations of fine- to medium-grained dolerite sills occur throughout the sequence, most commonly in rocks of the Callie boudin chert and Magpie schist, and are loosely grouped as the End-It-All Dolerite. Most of the sills are foliated by S_1/S_2 and thus are inferred to have been intruded before deformation. The sills are commonly associated with bedding-parallel strings of calc-silicate pods that are intensely recrystallized. Thin "glimmerite" or lamprophyre dykes locally cut across stratigraphy but are cut by ore-stage sheeted quartz veins.

Alteration and metamorphism

Although the rocks at the Callie deposit have undergone both metamorphic and hydrothermal alterations, the current mineral assemblages of the sedimentary rocks are relatively fine-grained, pseudomorphic textures are rare, and it appears that the alteration and metamorphic mineral assemblages are similar to each other and to the inferred original detrital mineral assemblage. It is therefore difficult to differentiate hydrothermal and metamorphic minerals from the detrital minerals. In general, detrital feldspar crystals, and possibly extremely fine-grained mafic mineral phases, have been progressively replaced by an assemblage of chlorite and biotite, with or without muscovite, during metamorphism and alteration. Because of this ambiguity, and because the major goal of this study is to identify the controls on gold mineralization, this description focuses on the observed mineralogical variations and their relationship to gold distribution rather than on the detailed mineralogical history of the rocks. A paragenesis of the main events, mineralization, and major mineral phases is shown in Fig. 5. The most distinctive mineralogical changes that appear to relate to the distribution of gold are depletion of graphite and the addition of chlorite, biotite, oxides, and sulfide minerals as discussed below.

Graphite

Graphite was originally a common component in all of the rock units within the Blake beds except the Lower Blake beds and Lower Blake laminations. Its detrital presence is indicated by remnant graphitic zones, certain textures (see below), and the presence of abundant graphite in the Callie laminated beds intersected in drill holes >500 m from the ore zones. Many of the rocks, however, have subsequently undergone either partial or complete removal of graphite. Figure 6a illustrates an instance where graphite has been completely removed on one side of a pre-ore quartz vein with no offset in bedding, and Fig. 6b shows progressive patchy graphite removal laterally along bedding. Beds in

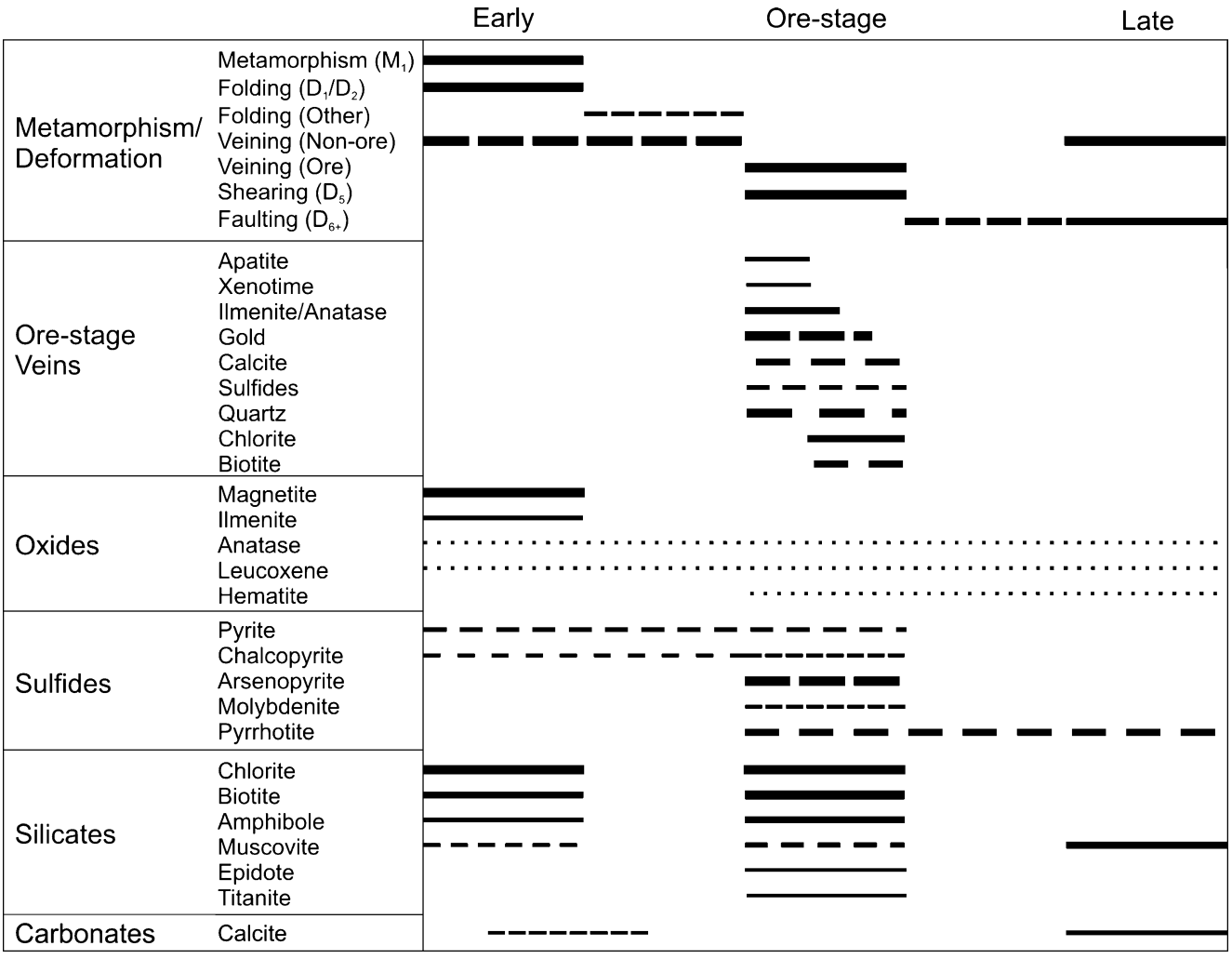

Fig. 5 Proposed paragenesis for host rock minerals, ore-stage veining, and structures at Callie. *Increasing line thicknesses* indicate increasing importance or abundance, *whereas increasing spacing of dashes or dots* indicates increasing uncertainty in the paragenetic timing. For clarity, neither diagenetic assemblages nor non-ore-stage veining episodes are included

which graphite has been removed tend to be paler in color than beds that were originally nongraphitic, and they commonly contain bedding-controlled concentrations of coarse biotite augen (described below; Fig. 6c).

The main ore zones at the Callie deposit are hosted in turbidites of the Callie laminated beds that have lost graphite as indicated by bleached bedding with coarse biotite augen. Rocks of the lower part of the Upper Blake beds, the Callie boudin chert, the Magpie schist, and the Callie laminated beds above and lateral to ore zones are overprinted by an irregular, poorly defined zone of partial graphite loss. All graphite-removal textures are observed in this zone, and coarse biotite augen are developed within those beds that are still partially graphitic (Fig. 6d). Graphite loss and associated textures are not, however, observed in these units on the limbs of the DBS anticlinorium distal to the ore zones. As graphite loss is localized within and adjacent to ore zones, this mineralogical change is interpreted to be associated with ore-related alteration, not metamorphism.

Biotite and chlorite

The dominant secondary mineral assemblages at Callie, particularly in and surrounding the ore zones, consist of abundant chlorite and biotite, with fine-grained muscovite identified by XRD in some samples. Chlorite is Fe-rich throughout (with anomalous deep blue interference colors), whereas biotite varies from Ti-rich (bright red interference color in thin section; Deer et al. 1992) near the ore zones to Ti-poor (green-brown color; Deer et al. 1992) below the ore zones. Four styles of Fe–Mg-bearing phyllosilicate assemblage are recognized: chlorite only, biotite only, biotite–chlorite, and magnetite–biotite–chlorite. The magnetite–biotite–chlorite assemblage only occurs lower in the stratigraphy of the Blake beds and is described in the next

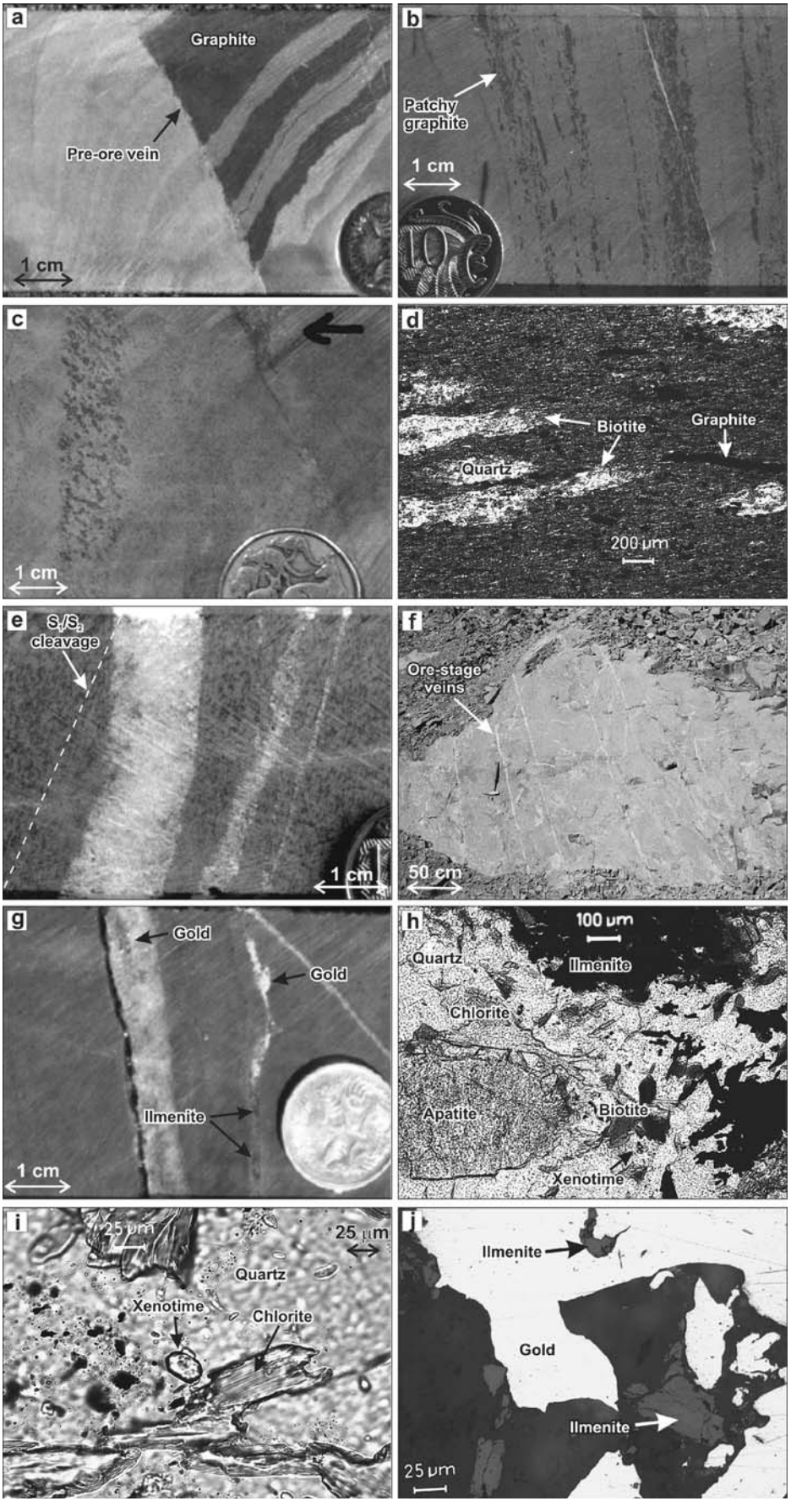
a
Graphite
Pre-ore vein
1 cm
b
Patchy graphite
1 cm
c
1 cm
d
Biotite
Graphite
Quartz
200 µm
e
S1/S2 cleavage
1 cm
f
Ore-stage veins
50 cm
g
Gold
Gold
Ilmenite
1 cm
h
100 µm
Quartz
Ilmenite
Chlorite
Apatite
Biotite
Xenotime
i
25 µm
25 µm
Quartz
Xenotime
Chlorite
j
Ilmenite
Gold
Ilmenite
25 µm

◀ **Fig. 6** **a** Decarbonization of continuous graphitic beds across a preexisting thin quartz vein that was impermeable to the hydrothermal fluids and prevented decarbonization to the right of the vein. There is no bedding offset across the vein (DBD417/667.6 m). **b** Partial decarbonization of graphitic beds in the lower portion of the Upper Blake beds. Bedding is readily apparent but only contains clots of relict graphite. The thin late-stage calcite vein is unrelated (DBD364/320.3 m). **c** Turbidite from the lower portion of the Upper Blake beds that shows spotty development of fine biotite augen throughout the sample. The band of coarse biotite augen development and bleaching is interpreted to have occurred in an originally graphitic bed, whereas the rest of the sample was originally nongraphitic and therefore was not as conducive to biotite growth (DBD364/262.2 m). **d** Transmitted light photomicrograph of large augen with quartz cores and coarse biotite rims in a partially decarbonized turbidite with relict clots of graphite. The augen are aligned with the original F_1/F_2 axial planar cleavage and are interpreted to have initially formed during metamorphism but were enhanced by coarse biotite growth during decarbonization by hydrothermal fluids resulting in the textures observed in (**c**) (DBD364/226 m). **e** Barren sheeted ore-stage quartz–biotite–chlorite veins of the QVC in the Callie laminated beds. The host rocks are strongly chloritic, with dark biotite augen. The similarity to the biotite band in (**c**) suggests that the host rock was also originally graphitic but has been decarbonized by the hydrothermal fluids. The veins occur at a slight angle to the S_1/S_2 cleavage defined by chlorite. The variation in vein orientation and thickness shown is common at centimeter scales, but the veins are planar and parallel at meter scales as shown in (**f**) (DBD395D5/886.0 m). **f** Outcrop view of at least five sheeted ore-stage QVC veins in the Wilson Shoot ore zone within the Callie laminated beds at the bottom of the Callie open pit. Although there may be local variations in orientation, the veins do not intersect with each other. **g** Two gold-bearing QVC veins. Some 1- to 2-mm clots of ilmenite are present within the veins, as well as apatite and xenotime. The host rock lacks coarse biotite and so may have been originally nongraphitic or lacked abundant K-silicate minerals or ferric iron (DBD395D3/899.0 m). **h** Transmitted light photomicrograph showing the assemblage of euhedral apatite, xenotime, and ilmenite within the gold-bearing quartz vein on the right in (**g**). This assemblage is only observed within ore veins containing visible gold (DBD395D3/899.0 m). **i** Transmitted light photomicrograph showing hydrothermal xenotime with chlorite in the gold-bearing quartz vein in (**g**) (DBD395D3/899.0 m). **j** Reflected light photomicrograph showing intergrown gold and ilmenite within the quartz–gold vein in (**g**) (DBD395D3/899.0 m)

section. Chlorite-only assemblages occur away from the ore zones, particularly in coarser grained rocks such as the Lower Blake beds, and in unmineralized Callie laminated beds >500 m from ore. Chlorite is extremely fine-grained (<10 μm) in the units stratigraphically above the Callie laminated beds where it gives the rocks a faint green coloration. Within the Callie laminated beds, Lower Blake laminations, and Lower Blake beds, chlorite is slightly coarser grained (20–75 μm), giving the rocks a strong green color and indicating a lithological control on chlorite abundance and crystal size.

The biotite-only zone is only present within partially decarbonized graphitic mudstone and turbidites between the Magpie schist and lower part of the Upper Blake beds, above the ore zones. The biotite in these rocks typically forms coarse biotite augen (≤2–3 mm) with small quartz cores (Fig. 6c,d). The biotite is coarser grained and more abundant in graphitic and decarbonized mudstone than in originally nongraphitic siltstone, even in adjacent beds. Rare, extremely fine-grained (<10 μm) chlorite may be present locally but is insignificant relative to the amount of chlorite present in the biotite–chlorite zones. The ore zones are generally associated with the biotite–chlorite assemblage in which host rocks have abundant coarse biotite augen (Fig. 6e) in an intensely chloritic matrix. Two stages of biotite growth are apparent. A common, fine-grained, anhedral stage, which in some rocks shows slight augen development parallel to the S_1/S_2 foliation, is overgrown by a coarser grained subhedral stage. The latter stage overprints the foliation and develops 2–3 mm augen (Fig. 6c–e). Chlorite replaces the fine-grained biotite but is overprinted by the coarser grained subhedral biotite. The spatial association of biotite augen and intense chloritization with ore, and their timing relative to pre-ore fabrics suggest an association with ore formation. The chlorite-only zones and the fine-grained stage of biotite growth are associated with pre-ore fabrics and are not spatially associated with ore, suggesting that they formed during regional metamorphism. Euhedral calcite crystals are a minor phase that locally crosscut chlorite and the coarser grained biotite augen and are inferred to be paragenetically late.

Oxide and sulfide minerals

The lower parts of the Lower Blake beds and Lower Blake laminations include barren zones of pervasive stratabound magnetite below the zone of auriferous sheeted veins. The magnetite zones could be at least partially responsible for the >45-km-long aeromagnetic anomaly that trends along the anticlinorium hinge. Core samples from the magnetite zones show magnetic susceptibilities up to 600×10^{-3} SI and average $10–60\times10^{-3}$ SI. Where graded beds are well developed, there is no clear relationship between host rock grain size and magnetite content. Nevertheless, the rocks in the magnetite zones are strongly banded parallel to bedding, with alternating chlorite- and magnetite–biotite-dominant bands ranging in thickness from several millimeters to 2–3 cm. Intermittent magnetite–quartz-dominant bands are also present. Two forms of magnetite are observed throughout: disseminated small (10–200 μm) euhedral magnetite crystals and larger (<1 mm) porphyroblastic magnetite grains with <50–100 μm inclusions of subhedral to euhedral silicates and pyrite. Radzik (1998) describes pronounced quartz pressure shadows surrounding the porphyroblastic magnetite grains, indicating that they formed pre- or syn-deformation. The chlorite-dominant bands contain disseminated subhedral to euhedral biotite crystals (<200 μm) and magnetite, all in textural equilibrium with a pervasive, moderately crystalline (<100 μm) chlorite groundmass. The magnetite–biotite-dominant

bands contain interlocking euhedral crystals of magnetite and Ti-poor biotite (<200 μm), which commonly share well-developed crystal faces, with lesser interstitial chlorite, again all in textural equilibrium. The magnetite–quartz-dominant bands have euhedral quartz (<150 μm) and magnetite with minor fine-grained chlorite and euhedral biotite (<50–100 μm). Although the magnetite-rich rocks are not noticeably foliated in hand sample, the biotite has a weakly to moderately developed preferred orientation in thin section. Minor ilmenite, pyrite, and local trace hematite are also present throughout. Where pyrite is present, it can be as coarse as 5 mm in diameter, always contains small euhedral magnetite inclusions, and may be intergrown with the porphyroblastic magnetite. Late-stage hematite rims are locally present on pyrite grains that contain inclusions of magnetite. Thin, early quartz veins are parallel to the banding which is strongly contorted as a result of rheological contrasts during deformation. Small breccia zones, in which magnetite forms part of both clasts and matrix, are present within magnetite-dominant bands.

Elsewhere in the stratigraphy at Callie, magnetite and hematite are absent; the only oxides observed are small (<1–2 mm) grains of ilmenite, with lesser rutile, leucoxene, and anatase. They are most commonly observed as clots of heavy mineral concentrations within some beds, most noticeably within the Callie laminated beds and, therefore, adjacent to the main ore zones.

Sulfide minerals are common in most units. Arsenopyrite is the most abundant sulfide in the sedimentary rocks and forms large (<10 mm) euhedral crystals. Other wall-rock sulfide minerals include, pyrite, pyrrhotite, rare but large (<10 mm) euhedral cobaltite (with the calculated formula $Co_{0.5}Ni_{0.3}Fe_{0.2}AsS$ from microprobe analyses), and trace molybdenite. Despite their common occurrence throughout the Blake beds, sulfide minerals are rare within the ore zones and are never found within 0.5–1.5 m of auriferous veins. Many sulfide grains (particularly pyrite and pyrrhotite) are elongate parallel to the S_1/S_2 cleavage, indicating that a proportion of sulfide minerals formed during or before F_1/F_2 folding. The majority of arsenopyrite, however, grows across the S_1/S_2 fabric, and the crystals commonly contain <100 μm inclusions of orthoclase, chlorite, albite, apatite, and calcite.

Calc-silicate pods

Calc-silicate pods are present throughout the stratigraphy at Callie and always correlate with negligible gold grades (<0.03 g/t) even where ore-stage sheeted veins are abundant. They range from 2–3 cm to 2–3 m in diameter and commonly occur in clusters near dolerite sills. They are rounded or ellipsoidal, but some elongate examples have been observed. The pods are commonly aligned along bedding planes, and core samples show the continuation of bedding through discordant pods, confirming that the pods formed by replacement after sedimentation. Two types of calc-silicate pods are present. A small proportion of the pods consist of unzoned, fine-grained rock comprising calcite, quartz, and minor calcic amphibole. The majority of pods, however, are zoned with dark rims, as much as several tens of centimeters wide, of coarse amphibole around a paler core. These pods contain calcic amphibole (10–60 vol.%), quartz (20–40 vol.%), carbonate (calcite with minor dolomite: 5–15 vol.%), clinozoisite (≤15 vol.%), and titanite (5 vol.%). Minor chlorite, ilmenite, rutile, and pyrite may also be present. Biotite, although common in surrounding rocks, is always absent.

The zoned pods commonly show at least two stages of amphibole growth, and possibly a third. Large (≤2–3 mm) bladed amphibole porphyroblasts form a strong foliation; however, several earlier porphyroblasts lie oblique to, and are crosscut by, this foliation. The large porphyroblasts commonly show patchy retrograde replacement by calcite. A later stage of amphibole growth, consisting of small radiating sheaves of acicular crystals, is observed in some samples, and small euhedral crystals overgrow and cut the margins of some of the large porphyroblasts. Haines (1999) observed that clinozoisite also showed two stages of growth. Given their multiple growth stages, common foliation, lack of gold, and their similarity to those observed within contact metamorphic aureoles surrounding granitic intrusions in turbidites of the Lachlan Fold Belt (Morand 1994), they are interpreted to be of intrusion-related origin before metamorphism and deformation and are unlikely to be associated with the mineralizing event at Callie.

Folding and faulting

The principal structural feature surrounding the Callie deposit is the tight, south–southeast-plunging, 3-km-wavelength, F_1 DBS anticlinorium; the deposit is located in the anticlinorium's 500-m-wide hinge zone (Fig. 3). Superimposed on the anticlinorium, and subparallel to its fold axis, are a series of tight, 150-m-wavelength, parasitic F_2 folds, which are interpreted to have formed during D_2 late in the Tanami orogenic event (Vandenberg et al. 2001). From south to north, these are named the Avon anticline, Jupiter 2 anticline, Marianas syncline, Callie anticline, Challenger syncline, and the Lantin anticline (Figs. 2 and 3). Gold ore zones are primarily located in the hinges of these anticlines. The Callie pit was designed to extract ore from the Wilson Shoot in the hinge of the Callie anticline, and underground mining has followed the ore zone across the Challenger syncline and into the hinge of the Lantin anticline.

Despite several deformation events that have affected the rocks at the Callie deposit, the dominant foliation is a

schistose cleavage that dips steeply south–southwest to south–southeast, depending on location, in a similar orientation to the axial planes of F_1 and F_2. Because the axial planes of F_1 and F_2 are also similar to each other, the main cleavage is referred to here as S_1/S_2 and is defined by trails of fine chlorite or by planes of elongate biotite augen. However, each individual biotite augen is slightly rotated with respect to chlorite/biotite planes; the largest apparent angle between the orientation of the biotite augen and the chlorite/biotite planes observed in thin section is about 20°. This rotation could have occurred during, or at any time after, the initial F_1 folding event and therefore remains unnamed but was probably associated with the growth of the biotite augen. Thin sections from graphitic rocks show weak development of an S–C fabric at an angle of about 40–45° surrounding quartz augen, but it is rare and not pervasive. The composite nature of the cleavage causes difficulties in measuring its orientation in drill core. By plotting the orientation of bedding on a stereo net, it is possible to estimate the general cleavage orientation and the orientation and shape of the anticlinorium (Fig. 7a). This S_1/S_2 cleavage persisted through subsequent deformations due to its strong mineralogical development during the most intense deformation phase. Subsequent deformations have merely warped and tightened the original F_1/F_2 folds and rotated the biotite augen.

The main structures that transect the F_1/F_2 folds are the D_5 quartz vein corridors (QVC) that host ore (below) and D_{6+} low-angle reverse faults (including the Servalan and Soolin Faults) and the Kerril Fault, which are all observed in the Callie pit (Figs. 2 and 3). The faults are all clearly late-stage features as they truncate or offset the ore zones and contain brittle fragments of occasionally auriferous sheeted quartz veins. The Kerril Fault is a zone of brittle crushed rock within and parallel to the ore zones, striking roughly east–west and dipping between 60 and 80° to the south with oblique dextral offset. Veining and alteration associated with faulting are restricted to local zones of intense, late carbonate–quartz veins that do not contain gold. Therefore, the Kerril Fault is interpreted to have overprinted existing gold mineralized rock, with no new introduction of gold.

Veining and gold mineralization

Gold at Callie is coarse and readily visible. It only occurs within veins within QVC; the main corridor, which hosts the Wilson ore shoot (Fig. 3), is a 150- to 180-m-wide and >1,000-m-long zone of strongly developed sheeted, en echelon quartz veins (Fig. 6e–g). Another two or three corridors are present locally but are narrower and less continuous (for details, see Voulgaris and Emslie 2004). The QVC trend roughly east–west and cut the F_1/F_2 folds but are cut by late D_{6+} faults so are attributed to D_5 shearing (Vandenberg et al. 2001). The shearing may be responsible for warping the anticlinorium from a south–southeast trend to a more east–west trend in the vicinity of the Callie pit and the QVC (Fig. 2). Gold, which pitches

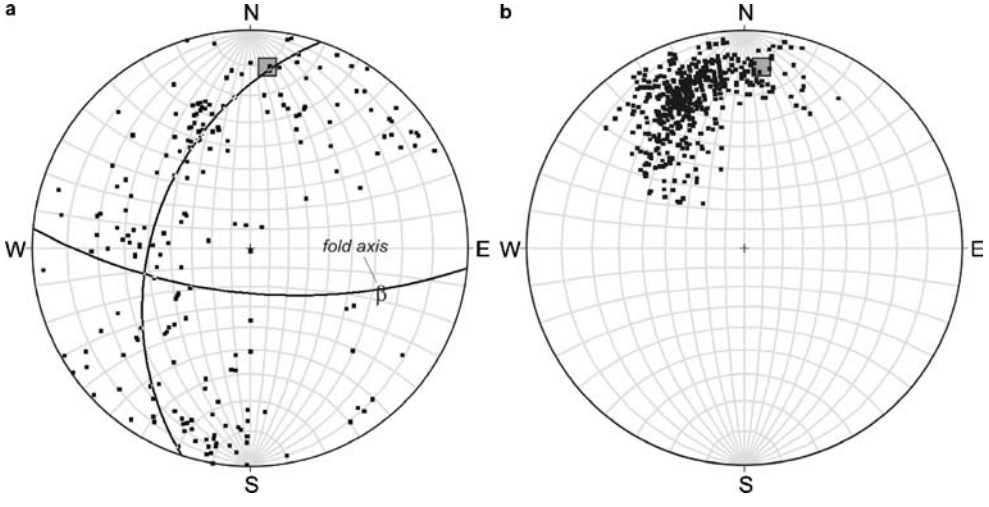

Fig. 7 **a** Lower hemisphere stereo net projection of a compilation of poles to bedding for 217 measurements taken from drill core and outcrops in this study and from Normandy NFM drill core logs (J. Emslie and D. Larsen, written communication 2001). Much of the scatter can be attributed to subsequent minor folding events and drill-core orientation problems; however, the main F_1/F_2 orientations dominate with a fold axis (point β) plunge/plunge-direction of 37→109, consistent with the observed fold trend (Figs. 2 and 3). The northerly trending great circle represents the girdle of best fit for poles to bedding, and the orthogonal easterly trending great circle represents the associated fold axial plane. The *gray box* shows the expected pole to the axial planar cleavage (095/73 S). **b** Lower hemisphere stereo net projection of poles to the ore-stage sheeted quartz veins. The average strike and dip is 070/63 SE for 557 points from drill core and outcrop in this study and Normandy NFM drill core logs (J. Emslie and D. Larsen, written communication 2001). The orientation of most veins is significantly different from that of the S_1/S_2 axial planar fold cleavage shown by the *gray box* from (**a**)

vertically within the veins, is present where the QVC veins cut fine-grained sedimentary rocks that have lost graphite during hydrothermal alteration. Gold is not present in the QVC veins where they cut dolerite sills, calc-silicate pods, lamprophyre dikes, or sulfide-bearing sedimentary rocks.

Both barren and auriferous ore-stage veins within the QVC have the same structural orientation and morphology. Both are typically 0.2–3 cm in width, with local pinch-and-swell textures, and extend for 5–10 m in length. They have sharp contacts with wall rock and tend to be planar and do not crosscut each other, making it impossible to ascertain the exact timing relationships. However, similarities in orientation, size, shape, and silicate mineralogy between auriferous and barren veins, and because both are only found within the QVC, suggest that they formed during a single event. Neither the auriferous nor the barren sheeted veins show discrete alteration selvages. Instead, the ore zones are characterized by tens of meters of decarbonized rock with a strong green chloritic tint and abundant coarse biotite augen.

Vein spacing varies significantly; ore zones commonly contain three to five veins per meter (Figs. 6f and 12) but may have up to 20 veins per meter. Higher densities of veining do not directly correlate with higher gold grades. The auriferous ore-stage quartz veins contain biotite, Fe-rich chlorite, calcite, gold, ilmenite, apatite, rutile, xenotime, and leucoxene but lack sulfide minerals. The barren ore-stage veins only contain biotite, Fe-rich chlorite, sulfide minerals, and minor calcite. Feldspar has been reported in the veins (Smith et al. 1998; Wygralak et al. 2004), but none was observed in this study. The large euhedral apatite (Fig. 6h), small euhedral xenotime crystals (Fig. 6h,i), Ti-oxides, and more abundant calcite found in the auriferous ore-stage veins are only found in close proximity to the gold grains, usually within 1–2 cm. Apatite and ilmenite also form the largest crystals within the auriferous veins and can be up to 1–2 mm across; they are much larger and have better defined crystal shapes than those that occur in the wall rocks. Chlorite shows pleochroic haloes where it contains, or lies adjacent to, xenotime crystals, and chlorite cleavage planes may be aligned subparallel to the margins of gold grains. In addition, ilmenite, which forms delicately bladed sheaves, is the only mineral to occur as inclusions within gold and is always surrounded by intergrowths of biotite and chlorite. These lines of evidence all suggest that the ilmenite, gold, apatite, and xenotime predate biotite and chlorite in the auriferous vein paragenesis. Despite this, the apatite and xenotime are unlikely to be detrital grains; xenotime has not been observed in any of the host rocks, and apatite is rare in the host rocks, but where it is found, it is always fine-grained and subangular. Their exclusive association with gold suggests a hydrothermal origin.

A variety of sulfide minerals are present within the barren ore-stage veins, including (in decreasing order of abundance) pyrite, pyrrhotite, chalcopyrite, arsenopyrite, and marcasite. The sulfide minerals are most common where the veins pinch inward. The same sulfide minerals also occur in the sedimentary rocks, away from auriferous ore-stage veins, where arsenopyrite is most abundant. Sulfide minerals are absent in auriferous ore-stage veins except for trace tetrahedrite enclosing gold in one sample. Within the QVC, there is a weak zonation of the sulfide minerals present in the barren ore-stage veins. Moving out laterally 10–100 m from the ore zones, the barren ore-stage veins commonly contain pyrite and pyrrhotite, but up to 50–150 m away, pyrite and chalcopyrite are more common. Higher in the stratigraphy, above the ore zones, barren ore-stage veins within the QVC dominantly contain quartz and sericite with few sulfide minerals.

Although sulfide minerals, especially arsenopyrite, are disseminated widely around the deposit (at distances of >1 km), at the stope or outcrop scale, there is an inverse relationship between the abundances of sulfide minerals and gold. Visible gold in the ore-stage veins is rarely observed within 0.5–1.5 m of sulfide minerals in either the wall rocks or the veins. This inverse relationship is also demonstrated by the abundance of SO_3 in the geochemistry (below and Fig. 12). Smith et al. (1998) and Haines (1999) have noted that gold is concentrated where veins intersect bedding planes, although this relationship was not observed in this study.

Fraser (2002) used $^{40}Ar/^{39}Ar$ geochronology of biotite to date a biotite-rich lamprophyre dyke at ~1,760 Ma. As this dyke is cut by a barren ore-stage vein, the age was interpreted by Fraser (2002) to provide a maximum age for the veins. Additional $^{40}Ar/^{39}Ar$ dating of biotite from within barren ore-stage sheeted veins gave ages of ~1,720 Ma (Fraser 2002) consistent with the observed crosscutting relationship. In situ SHRIMP U–Pb analyses of hydrothermal xenotime associated with gold (see above), however, gave an age of 1,803±19 Ma (Cross et al. 2005). Although this age is significantly younger than the inferred Dead Bullock Formation sedimentation age of 1,838±6 Ma (Cross and Crispe 2006), consistent with a hydrothermal origin for the xenotime, it is inconsistent with the $^{40}Ar/^{39}Ar$ ages of Fraser (2002). At this writing, this conundrum is unresolved. However, xenotime U–Pb dating is considered more robust due to the higher closure temperature of U–Pb in xenotime, the xenotime age at Callie is within error of a xenotime age obtained for the nearby Coyote gold deposit (~1,793 Ma: Bagas et al. 2006), and Pb–Pb model ages for galena in late-stage quartz-carbonate veins at Callie (see below) yielded an age ~1,801 Ma (Huston et al. 2006), with the ~1,803 Ma xenotime age being considered most reliable for the age of mineralization. This leaves the possibility that the $^{40}Ar/^{39}Ar$ ages presented by Fraser (2002) represent the age of the barren ore-stage veins; however, no crosscutting relationships are present to confirm this hypothesis.

A compilation of the orientations of the barren and auriferous sheeted quartz veins from this study and from Normandy NFM logs (J. Emslie and D. Larsen, written communication 2001) indicates that their average strike and dip is 070/63 SE (557 points) with significant scatter (Fig. 7b). Although slight variations in vein orientation are observed in the field (e.g., Fig. 6e), some of the scatter is probably a consequence of poorly orientated drill core and the problems associated with data collection from drill core. Some of the veins appear to form parallel to the S_1/S_2 fold cleavage, but most form at an acute angle to the S_1/S_2 cleavage as observed in hand samples and by comparison of Fig. 7a and b.

Several other types of veins that are unrelated to the QVC are present at Callie, having formed before or after the mineralization event. There are early thin (<5 mm but commonly 1–2 mm), commonly ptygmatic, quartz veins that are generally parallel to bedding and include minor chlorite, pyrite, and chalcopyrite. They have been deformed and folded with the rocks so predate D_1. Unoriented quartz veins of varying thickness, commonly with abundant biotite, chlorite, and sulfide minerals, are common and are mineralogically similar to the barren ore-stage veins. Late-stage calcite–quartz and ankerite–quartz veins cut the ptygmatic and ore-stage veins and all structural fabrics and faults, including the D_{6+} structures. These veins commonly contain sulfide minerals, including sphalerite, pyrrhotite, galena, and pyrite and have well-developed carbonate and sericite alteration selvages <5–10 cm wide. A final stage of buck quartz veining was described by Smith et al. (1998). Within and adjacent to the magnetite zones in the Lower Blake beds, there are thin (1–2 mm) calcite–magnetite–hematite–chalcopyrite veins at various orientations with strong chlorite–biotite destructive sericitic selvages; their timing, however, is not known.

Geochemistry

To determine possible geochemical controls on gold precipitation, the geochemistry of the stratigraphic sequence hosting the Callie deposit has been determined from samples collected from diamond drill core. The hydrothermal apatite, ilmenite, and xenotime observed in gold-bearing veins suggest that several elements that are commonly considered immobile, Ti, Y, and P (Cann 1970), have been mobilized to some extent by hydrothermal fluids. Geochemical approaches using immobile element geochemistry to quantify mass changes associated with hydrothermal alteration will be of limited use. The bulk chemistry of the 163 sedimentary rock samples (which exclude samples containing calc-silicate pods, intrusions, or intense late carbonate veining) from Callie is reflected in Fig. 8, a modified ACF diagram (after Nesbitt and Young 1989; and Bierlein et al. 1998). The Callie sedimentary rocks are Fe- and Mg-rich, with an average FeO^T of 12.7 wt% (range 5.6–28.3 wt%) and an average MgO content of 3.7 wt% (range 1.3–9.8 wt%) compared to average shale values of 6.0 and 2.5 wt%, respectively (Mason 1982). The samples therefore trend toward chlorite and biotite compositions, consistent with the observed chlorite–biotite alteration/metamorphic assemblages. There is a lesser trend of carbonation heading toward calcite and dolomite. Neither of these trends is closely associated with high gold grades, and there is no indication of significant sericitization or K-metasomatism. The geochemistry confirms that bleaching associated with ore zones is caused by the loss of graphite during hydrothermal alteration. Carbon contents decrease from up to 2.0 wt% in nonmineralized zones 10–50 m from ore zones to <0.01 wt% in the bleached fine-grained rocks of the Callie laminated beds within ore zones (Fig. 12). The minimum carbon content measured in rocks that contain a small amount of visible graphite is 0.03 wt%.

Correlation analysis was used to assess possible geochemical trends associated with Au and alteration of the Callie sedimentary rocks. In addition to the major and trace elements, the correlation analysis included several alteration indices commonly applied to gold deposits: K_2O/Na_2O and the molar ratios Na/Al and 3K/Al (Eilu et al. 1997) to assess alkali alteration, and the molar ratios CO_2/Ca and CO_2/(Ca+Mg+Fe−S) to assess carbonation (Eilu et al. 1995, 1997). The CO_2/Ca ratio is 1 for calcite, 2 for ankerite or dolomite, and infinite for siderite, so it can help identify which carbonate phases are dominant, if any. The CO_2/Ca values at Callie average 0.47±0.77 (2σ), with only 12 of the 163 samples ≥1.0, indicating that silicate minerals host most of the Ca, consistent with the petrography. The CO_2/(Ca+Mg+Fe−S) ratio, which is 1 for all carbonates, assesses the availability of Ca, Mg, and Fe (with a correction for iron locked up in arsenopyrite and pyrrhotite) for carbonate formation; low values indicate that CO_2 was the limiting component whereas high values indicate that Ca, Mg, and Fe were the limiting components. At Callie, the CO_2/(Ca+Mg+Fe−S) ratio averages 0.05±0.15 (2σ), indicating that the rocks were strongly undersaturated with CO_2. Several redox-sensitive element ratios were also used to attempt to identify any redox changes in the rocks: U/Th and V/Cr (Jones and Manning 1994), V/(V+Ni) (Lewan 1984), V/Sc (Kimura and Watanabe 2001), FeO/(FeO+Fe_2O_3), and C/(C+CO_2). All redox ratios are posed such that more reduced rocks have higher values. Changes in concentrations of the redox-sensitive elements Cr, V, Mo, and U, which form insoluble compounds under reduced conditions, and Cd, Cu, Ni, and Zn, which form highly insoluble sulfide minerals under reduced conditions (Calvert and Pederson 1993), are also used to monitor

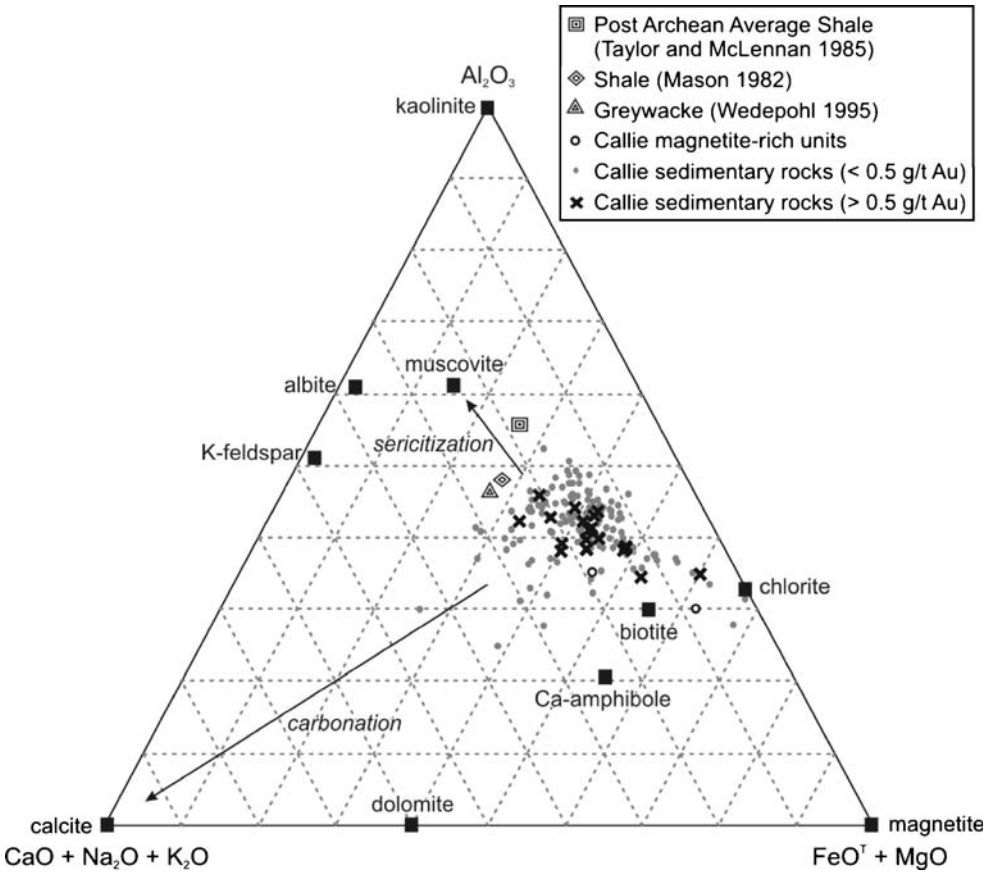

Fig. 8 ACF-type diagram showing the bulk composition of all 163 sedimentary rock samples. Mineral compositions were all measured by electron microprobe on Callie samples, except kaolinite and dolomite which were not observed. The Callie sedimentary rocks are enriched in FeO^T and MgO relative to several average shale and graywacke compositions and trend toward chlorite and biotite, the dominant mineral assemblage. Some samples also show carbonation, but there is no evidence of sericitization or K-metasomatism. Mineralized samples do not show any major difference from the barren samples in their bulk composition. After Nesbitt and Young (1989) and Bierlein et al. (1998)

redox changes in the rocks with higher abundances indicating more reduced conditions.

The results of the correlation analysis are summarized in Table 1. All correlations shown are significant at the 95% confidence interval for the relevant number of samples. On each line, the major elements, trace elements, and ratios are sorted in the order of decreasing strength of correlation. The most obvious alteration in the Callie rocks is decarbonization, and correlation analysis of 57 samples with >0.03 wt% C (enough to contain visible graphite) or partial or complete decarbonization textures (patchy graphite within beds, or coarse bands of biotite augen with bleaching) shows that the loss of C corresponds with a clear change to more oxidized rocks with a decrease in most of the redox-sensitive indicators: U, Cd, Zn, Mo, V/Sc, $C/(C+CO_2)$, V/Cr, and V/(V+Ni). The correlation analysis also shows that decarbonization and carbonation are not directly linked: decarbonization does not correlate with either of the carbonation indices or addition of CO_2. The observed decrease in $C/(C+CO_2)$ is therefore most likely controlled by the loss of C rather than the addition of CO_2 in these samples. The other redox-sensitive indicator, $FeO/(FeO+Fe_2O_3)$, does not show a significant correlation with either C or CO_2 but does show a strong negative correlation (exceeding the 99% confidence interval) with $C/(C+CO_2)$ (Fig. 9). The proportion of Fe^{2+} in the rocks increases as the proportion of organic carbon decreases. The typically immobile elements, TiO_2, Al_2O_3, Zr, Hf, Y, and HREE, all show positive correlations with decarbonization due to passive enrichment associated with a decrease in the mass of the rocks; SiO_2 and SO_3 may also be lost with C.

In the 19 most Au-rich (>0.5 g/t) samples, there are few correlations with Au aside from the expected relationship with Ag, which has a maximum abundance of 0.6 g/t. The Au-rich samples are associated with elevated Fe_2O_3 and diminished $FeO/(FeO+Fe_2O_3)$. As there is no enrichment of FeO^T+MgO in Au-rich samples (Fig. 8) and no compensating depletion in MgO (Table 1), decreases in $FeO/(FeO+Fe_2O_3)$ ratio probably represent a change in the iron oxidation state from Fe^{2+} to Fe^{3+} due to oxidation of the rocks during the most intense mineralization (Fig. 10a and below). This is in contrast to the increase in Fe^{2+} observed with decarbonization.

When looking at correlations with Au in all 163 sedimentary rock samples, many more relationships appear to be present, but many reflect variations in the host rock compositions as gold preferentially occurs in the Callie laminated beds and the Lower Blake laminations. The Au-bearing rocks show higher Na_2O and Na/Al, and lower K_2O/Na_2O, counter to their behavior in many lode gold deposits and consistent with the lack of sericitization or K-metasomatism observed at Callie. There is a correlation

Table 1 Geochemical correlations in sedimentary rock samples from Callie

Association	Elements	Positive	Negative
Gold (as Au); 19 samples with >0.5 g/t Au	Major	Fe_2O_3	–
	Trace	Ag, Sr	–
	Alteration	–	–
	Redox	–	$FeO/(FeO+Fe_2O_3)$
Gold (as $\log_{10}$ Au); 19 samples with >0.5 g/t Au	Major	Fe_2O_3	–
	Trace	Ag, Cs, Cu	–
	Alteration	–	–
	Redox	U/Th	$FeO/(FeO+Fe_2O_3)$
Gold (as Au); all 163 sedimentary rock samples	Major	–	–
	Trace	Ag, Sc	–
	Alteration	–	–
	Redox	U/Th	–
Gold (as $\log_{10}$ Au); all 163 sedimentary rock samples	Major	$\log_{10}$ CaO, Na_2O, CO_2, $\log_{10}$ MnO	C, $\log_{10}$ SO_3
	Trace	Ag, Ni, Sc, Sb, V, Cu, Cr	LREE, Ta, Nb, Th, Rb, Zr
	Alteration	Na/Al, $CO_2/(Ca+Mg+Fe-S)$	La/Sm, K_2O/Na_2O, S/As
	Redox	U/Th, $FeO/(FeO+Fe_2O_3)$	$C/(C+CO_2)$, V/(V+Ni)
Decarbonization (as C loss); 57 graphitic or decarbonized samples	Major	TiO_2, MgO, Al_2O_3, FeO, Na_2O	SiO_2, SO_3
	Trace	HREE, Sc, Y, Zr, Hf	U, Cd, Zn, Th, Mo
	Alteration	–	La/Sm, K_2O/Na_2O, 3K/Al, S/As
	Redox	–	V/Sc, $C/(C+CO_2)$, V/Cr, V/(V+Ni)
Carbonation [as $CO_2/(Ca+Mg+Fe-S)$]; all 163 sedimentary rock samples	Major	CO_2, CaO, MnO, SO_3	Al_2O_3, TiO_2, FeO, MgO, K_2O, $\log_{10}$ Fe_2O_3
	Trace	Sr, Eu, Mo, Bi, Pb, Cd, $\log_{10}$ As, $\log_{10}$ Au	Ta, F, Nb, Hf, HREE, Zr, Sc, Sn, V
	Alteration	CO_2/Ca, Na/Al	–
	Redox	U/Th, V/Sc	$C/(C+CO_2)$, V/Cr

All correlations are significant at the 95% confidence interval for the relevant number of samples and are sorted by decreasing significance on each line. The 19 au-rich samples and the 57 graphitic and carbonized samples are subsets of the 163 sedimentary rock samples.

between Au and carbonation, with elevated CaO, CO_2, CO_2/(Ca+Mg+Fe-S), and MnO, but the fact that gold occurs in decarbonized rocks with low C (typically <0.05 wt%) and $C/(C+CO_2)$ ratios (typically <0.2) is also evident (Figs. 9 and 10b). The carbonation in these samples shows a negative correlation with TiO_2, Al_2O_3, Zr, Hf, Y, and HREE due to passive depletion with the addition of carbonate. The change in redox state caused by carbonation is ambiguous: Mo, Cd, U/Th, and V/Sc are enriched, whereas V and V/Cr are depleted; however, the indicators may respond at different redox levels.

An additional trend in sulfur is observed with increasing Au grades in all rocks: both SO_3 and the molar ratio S/As decrease (Fig. 11). The S/As ratio gives an indication of the proportion of arsenopyrite present in the sulfide assemblage; a ratio of 1 indicates that pure arsenopyrite is the only sulfide. Although As contents are similar in all the Callie sedimentary rocks regardless of Au grades (average 529 ppm; Fig. 11b), the 19 Au-rich rocks at Callie have S/As ratios averaging 12±27 (2σ) with an average of 0.18±0.29 (2σ) wt% SO_3 whereas the rest of the rocks have average S/As ratios of 89±559 (2σ) and an average of 0.45±0.90 (2σ) wt% SO_3 (Fig. 11a,c). Sulfidation reactions are therefore unlikely to have caused Au precipitation, and sulfide minerals are not expected to be common in ore zones; however, arsenopyrite is expected to be common where sulfide minerals are present, consistent with the observed sulfide distribution.

Although Fe_2O_3 is enriched and $FeO/(FeO+Fe_2O_3)$ is depleted with increasing Au in the 19 Au-rich rocks, the converse is true when looking at all of the rocks (Fig. 10a). Low Au grades (<0.5 g/t) occur in rocks with a broad range of $FeO/(FeO+Fe_2O_3)$ ratios, but elevated Au grades only occur in those rocks with $FeO/(FeO+Fe_2O_3)$ ratios >0.8, so Au is found in the rocks containing the most reduced iron. This is consistent with the elevated redox-sensitive indicators Ni, V, Cu, Cr, and U/Th associated with increasing Au in all samples (Table 1). However, at the highest Au grades, there is a pronounced decrease in $FeO/(FeO+Fe_2O_3)$ suggesting that the associated hydrothermal fluids oxidized iron in the host rocks. It is important to note that the barren banded magnetite samples have the lowest

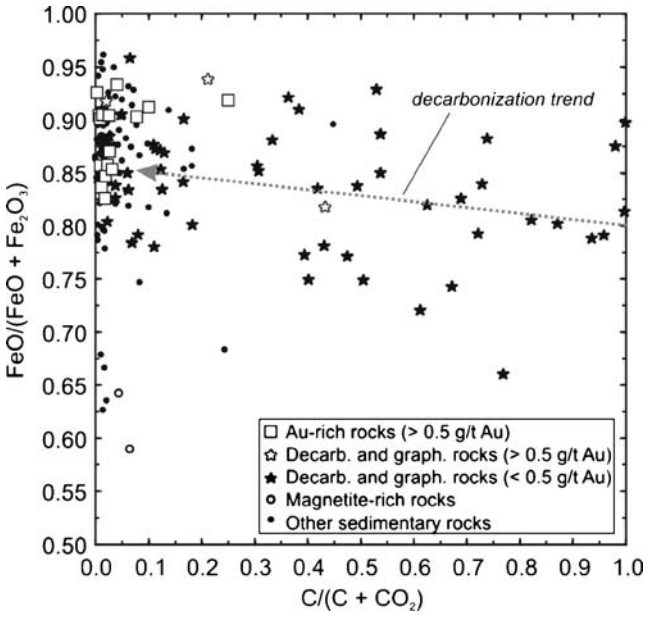

Fig. 9 Plot of $C/(C+CO_2)$ vs $FeO/(FeO+Fe_2O_3)$ for the 163 sedimentary rock samples, broken into groups. The decarbonized and graphitic rocks consist of 57 samples that either contain >0.03 wt% C (enough to be visible as graphite), or clear decarbonization textures such as patchy graphite, or bands of coarse biotite augen in bleached beds. Although other samples may have undergone decarbonization, they lack definitive evidence for it. The decarbonized and graphitic rocks show a strong negative correlation between $C/(C+CO_2)$ and $FeO/(FeO+Fe_2O_3)$, at greater than the 99% confidence interval, with the linear regression line shown by the *arrow*. The 19 Au-rich samples are shown with *squares* and *open stars*. The range in $FeO/(FeO+Fe_2O_3)$ values shown in the Au-rich samples reflects the decrease in $FeO/(FeO+Fe_2O_3)$ associated with increasing Au grades shown in Fig. 10a

$FeO/(FeO+Fe_2O_3)$ ratios and therefore have the most oxidized iron of any of the rocks (Fig. 10a).

The geochemical alteration is summarized in Fig. 12 which shows the down-hole geochemistry and geology for hole DBD395D5 passing through the main Wilson Shoot ore zone in the hinge of the Lantin anticline on the 602000 mE section. The units to the south of the south-dipping Kerril Fault are faulted down (apparent normal offset) and as a result, some decarbonized Upper Blake beds from just above the hinge of the anticline are brought down into contact with the mineralized Callie laminated beds. The fault zone truncates the ore zone and contains broken pieces of auriferous sheeted quartz veins. The QVC in this hole extends from about 840 to 950 m, which corresponds well with the zone of most intense alteration. The altered rocks within the QVC and around the ore show: a depletion in organic C from 0.1 wt% at the interval margins down to <0.02 wt% in the ore zone; low levels of carbonation; $FeO/(FeO+Fe_2O_3)$ ratios above 0.8 with a slight decrease in $FeO/(FeO+Fe_2O_3)$ ratios within the ore zone; low SO_3; and low K_2O/Na_2O (with the exception of a zone of low Na_2O associated with the down-dropped section of Upper Blake beds). The elevated SO_3 and CO_2 at 870 m is associated with late carbonate–quartz–pyrite–pyrrhotite veining in the Kerril Fault. Similar veining was logged between 900 and 910 m corresponding to the sharp spike in SO_3 and CO_2.

To help assess the origins of the magnetite zones below the deposit and establish possible links to mineralization, a study of the magnetite compositions was undertaken. A compilation of 54 microprobe analyses of magnetite from the magnetite zones from Radzik (1998) and 48 from this study (including 24 trace element analyses) shows only trace impurities. There is no clear difference in chemistry between the disseminated or porphyroblastic styles of magnetite. The most abundant impurities are Si (average of 930 ppm) and V (average of 850 ppm). The abundances of Ti, Al, and Cr are commonly <300 ppm, and Mn, Cu, Zn, Mg, and Ca are consistently below detection levels (<50–200 ppm).

Carbon isotopes and fluid inclusions

Carbon isotope analyses on 11 samples of variously altered sedimentary rocks that contained enough carbon for reliable analysis showed $\delta^{13}C_{PDB}$ ranging from −26.0 to −22.4‰ (average=−24.1‰; Table 2). Although there is a bias toward less altered samples that still contain enough graphite for analysis, no correlation was noted between $\delta^{13}C_{PDB}$, carbon content, geological unit, or location relative to the ore zones.

Wygralak et al. (2004) document two types of coexisting fluid inclusions in ore-stage quartz veins at Callie: CO_2-rich and H_2O-rich. The CO_2-rich inclusions have high degrees of fill ranging from 50 to 100 vol.% CO_2 and have homogenization temperatures of 254–326°C with salinities of 4–7 wt% NaCl equivalent. Mernagh and Wygralak (2006, in review) report that the CO_2-rich inclusions contain up to 76 mol% (median 17 mol%) N_2 and up to 12 mol% (median 2 mol%) CH_4. The H_2O-rich inclusions homogenize over similar temperatures of 209–404°C with salinities of 7–20 wt% NaCl equivalent. Based on these two types of inclusions, they proposed that phase separation may have occurred with the trapping of two immiscible fluids and that the gas-rich inclusions formed at a depth of 2.3–6.0 km. Their fluid inclusion data do not indicate any difference in fluids between barren and gold-bearing ore-stage veins.

Discussions

This study has identified a range of structural and geochemical characteristics at Callie, which may have controlled mineralization. In the following section, these characteristics

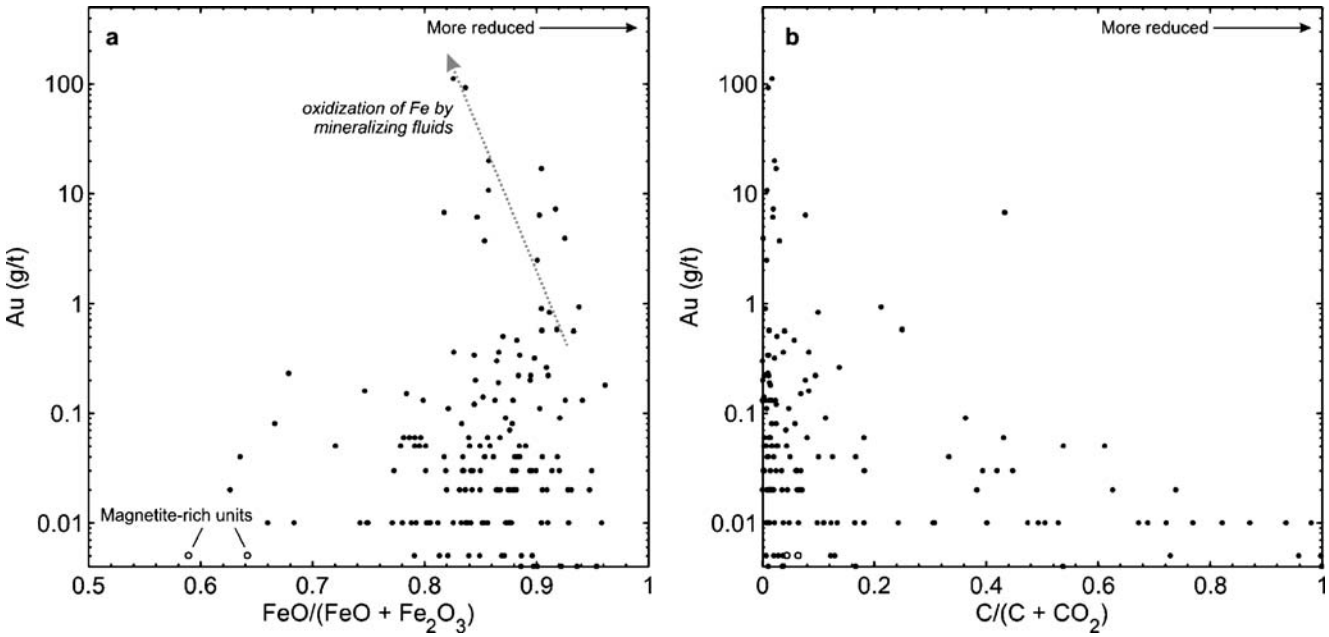

Fig. 10 Plots of Au vs $FeO/(FeO+Fe_2O_3)$ (**a**) and Au vs $C/(C+CO_2)$ (**b**) showing that significant Au (>0.5 g/t) only occurs in rocks with $FeO/(FeO+Fe_2O_3)$ ratios >0.8 and low $C/(C+CO_2)$ ratios <0.2. Both relationships can be explained by reactions that liberate C from graphite into CO_2, causing low $C/(C+CO_2)$ ratios, by reducing the ferric iron component of the rocks to ferrous iron in biotite and chlorite, causing high $FeO/(FeO+Fe_2O_3)$ ratios. The barren magnetite-rich samples have the lowest $FeO/(FeO+Fe_2O_3)$ values. In the most Au-rich samples, there is a noticeable decrease in $FeO/(FeO+Fe_2O_3)$ with increasing gold grade above 0.5 g/t. This indicates a slight oxidation of ferric iron to ferrous iron by the most mineralizing fluids. This additional control by slightly oxidized fluids may have contributed to the high gold grades in these samples

are assessed to establish the main controls on mineralization. Structural factors considered include stress regimes and metamorphic conditions at the time of mineralization and the influence of preexisting structures in localizing gold deposition. Chemical factors considered include the roles of decarbonization, fluid reduction, and sulfidation reactions. The relative importance of each of these features is assessed on the results of structural analysis, petrography, and geochemistry presented in this study.

Structural controls on mineralization

It is apparent from the petrography (particularly the two main growth stages observed for biotite and amphibole, and possibly for chlorite and clinozoisite) and morphology of the deposit that there were two main thermal events: an initial lower greenschist facies metamorphic and deformational event and a later hydrothermal event. Both resulted in the development of chlorite–biotite mineral assemblages with some slight petrographic differences. The regional structural history (Vandenberg et al. 2001) and previous work at Callie (Smith et al. 1998) suggest that these two events may correspond to the D_1/M_1 Tanami Orogenic Event (~1,835–1,825 Ma: Vandenberg et al. 2001; and Crispe et al. 2006) and a D_5 hydrothermal event.

Textural relationships, the crosscutting nature of the QVC with respect to the folds of the DBS anticlinorium, and the distinct difference in angle between the sheeted veins and the anticlinorium cleavage (Fig. 7) indicate that the development of the QVC and mineralization occurred after all major folding events but before the late D_{6+} faults. The style and orientation of the veins in the QVC are consistent with those that develop in semibrittle sinistral shear zones (Fig. 13; Davis and Reynolds 1996; L. Vandenberg, personal communication 2001), and based on the orientation of the veins, it is proposed that the QVC developed with sinistral strike-slip strain during east–northeast-oriented D_5 compression under semibrittle conditions (Vandenberg et al. 2001). This sinistral strain may also have been accommodated by the local warping of the F_1 anticlinorium from a southeast orientation (Fig. 2, top left) into a more east–west orientation in the vicinity of the Callie pit and QVC (Fig. 2, center). With elevated pore fluid pressure from hydrothermal fluids and low strain rates, strain would have been accommodated by the opening of the sheeted en echelon vein sets in the QVC. Smith et al. (1998) suggested that the common unoriented quartz veins that are mineralogically similar to the sheeted quartz veins formed with increasing fluid pressure early in D_5 before development of the stress regime responsible for the sheeted veins. Although the Kerril Fault runs subparallel to the QVC, its apparent oblique dextral offset, truncation of ore zones, inclusion of brittle fragments of gold-bearing sheeted quartz veins, and lack of mineraliza-

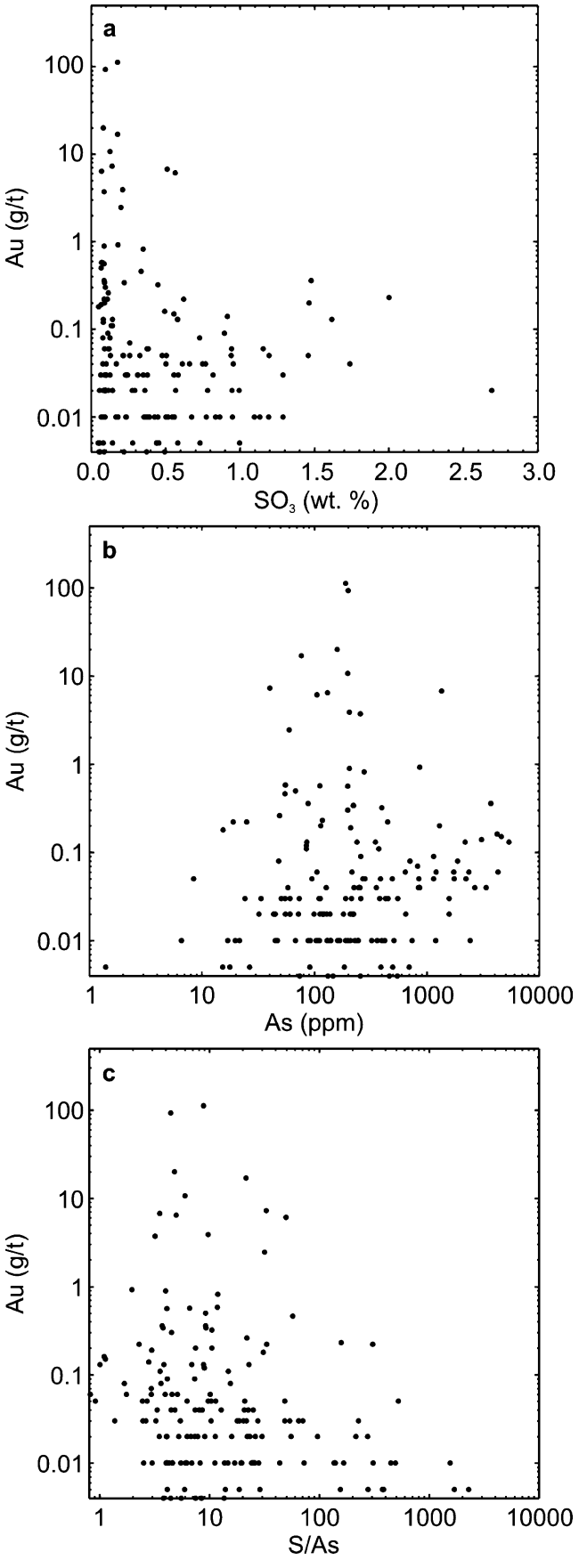

◀ **Fig. 11** Plots of SO_3 vs Au (**a**), As vs Au (**b**), and molar S/As vs Au (**c**) showing how the most mineralized rocks have the least SO_3 yet As contents are relatively similar regardless of Au content (average 529 ppm). As a result, low S/As ratios (averaging 12) are expected adjacent to ore zones, corresponding to abundant arsenopyrite, but the lack of SO_3 within the ore zones indicates a lack of sulfide minerals near gold and that sulfidation reactions did not cause gold precipitation

tion-related alteration or veining within it suggest that it is a late structural feature that exploited the preexisting weakness of the QVC and was not associated with mineralization. During D_5, hydrothermal fluids are interpreted to have flowed into dilational zones within the QVC; however, the concentration of ore in the hinges of the F_1/F_2 folds (Figs. 3 and 12) suggests that rising fluids were channeled into the closures of anticlines (cf. Ferry 1992) where finer grained beds impeded fluid outflow ensuring time for efficient chemical reaction. The intersection of the QVC with the DBS anticlinorium is considered to be essential in the development of the Callie deposit (see also Huston et al. 2006 for a review).

Chemical controls on mineralization

Extensive, magnetite-rich zones are developed below the ore zones along the hinge zone of the DBS anticlinorium. The magnetite is at least partially responsible for the >45-km-long magnetic anomaly tracing the hinge of the anticlinorium; the anomaly is thought to occur where folded magnetite-bearing rocks occur at shallow levels. A second magnetic anomaly of similar length, amplitude, and orientation runs subparallel to the first, about 10 km to the northeast, and is also attributed to Dead Bullock Formation rocks (Vandenberg et al. 2001). The magnetic anomalies are clearly regional features suggesting a lithological control on the magnetite distribution. Fine layer–parallel changes in magnetite abundances within the magnetite zones indicate that magnetite formation is controlled by fine lithological changes, likely the detrital abundance of iron, in the host sediment. Textural relationships, including the development of porphyroblastic grains in equilibrium with surrounding silicates, the development of quartz pressure shadows, and the brecciation of magnetite-bearing zones, suggest that the magnetite zones developed during metamorphism and deformation. The magnetite is chemically pure, a characteristic of BIFs or pelitic metasedimentary rock (Rumble 1976; Frost 1991), whereas hydrothermal magnetite tends to have high concentrations of trace elements (Lovering and Hedal 1987). The magnetite zones are therefore inferred to have formed from metamorphism of nongraphitic, Fe-rich sedimentary rocks or perhaps proto-iron formations. Although the magnetite zones are not interpreted to have formed in the lode gold mineral system, they would have

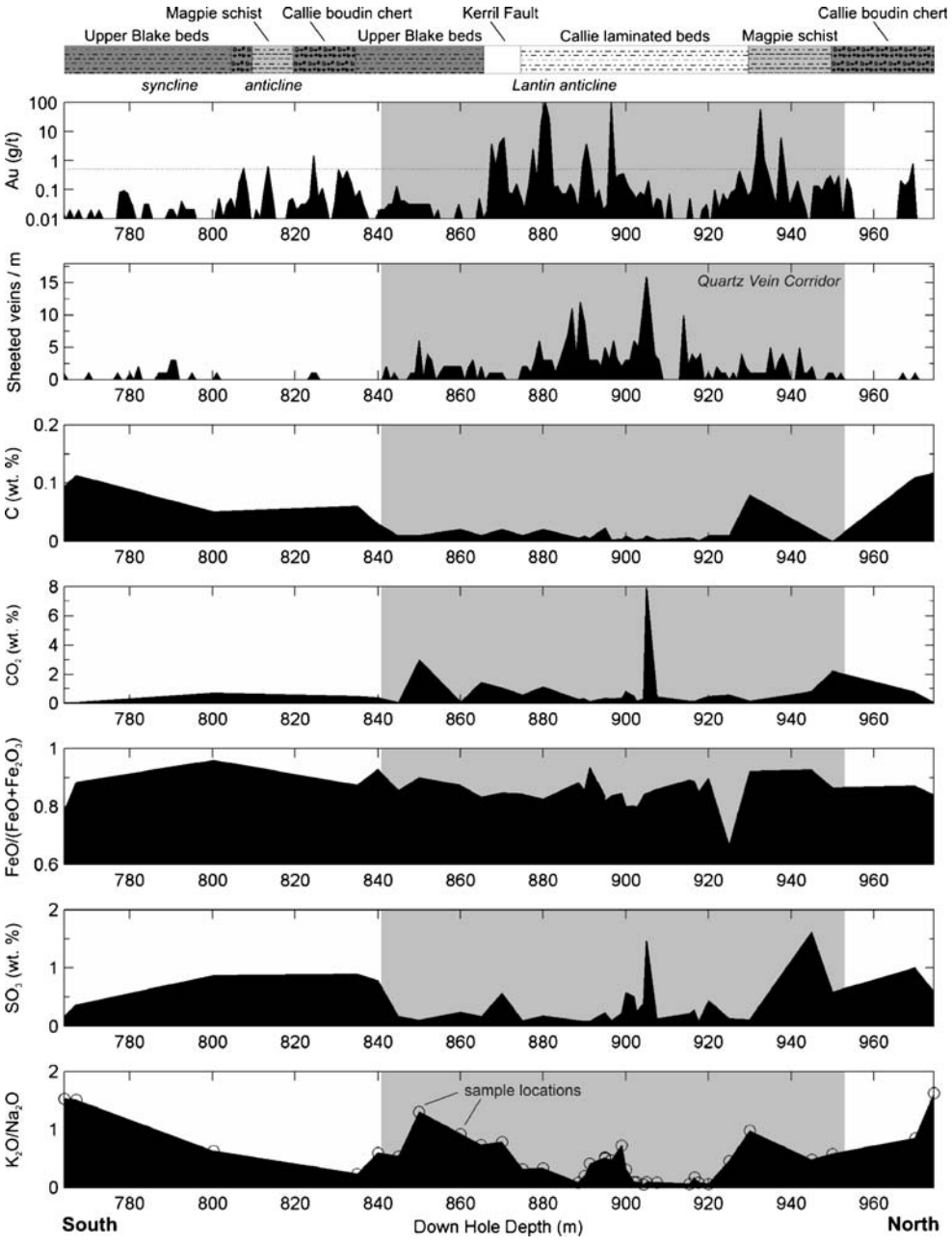

Fig. 12 Down-hole plots of geology and alteration geochemistry for DBD395D5 on the 602000 mE section. The hole passes through the Wilson Shoot QVC in the hinge of the anticlinorium at the level of the Callie laminated beds. Late, apparent normal, offset along D_{6+} Kerril Fault has down-dropped some decarbonized Upper Blake beds from higher in the fold hinge into contact with the Callie Laminated beds. The QVC, shown in *gray* and defined by an abundance of ore-stage veins (either barren or auriferous), is associated with decarbonization of the host rocks, low carbonation, high $FeO/(FeO+Fe_2O_3)$ >0.8, low SO_3 (and a lack of sulfide minerals), and low K_2O/Na_2O. The most mineralized samples (plotting above the 0.5 g/t Au cutoff line), however, show a slight decrease in $FeO/(FeO+Fe_2O_3)$ due to slight oxidization of the rocks by a relatively oxidized fluid. Gold assays and vein densities are generally on 1-m intervals, and the locations of 35 whole rock geochemical analyses are shown on the bottom plot. The geological units are depicted as in Fig. 4, with their typical abundance of graphite indicated by shading

buffered subsequent ore fluids during their ascent to the depositional site. The rims of pyrite and hematite surrounding some magnetite grains could be of hydrothermal origin, but the lack of obvious hydrothermal modification of the magnetite suggests that the fluid was mainly in equilibrium with magnetite (Fig. 14; Huston et al. 2006).

The primary chemical control on gold deposition is suggested by low $C/(C+CO_2)$ ratios and high $FeO/(FeO+Fe_2O_3)$ ratios in ore zones. The transition from nongraphitic decarbonized rocks with low $C/(C+CO_2)$ in ore zones through an irregular zone of partial decarbonization and into relatively unaltered graphitic rocks with high $C/(C+CO_2)$ above the ore zone is inferred to be the result of a diffuse hydrothermal decarbonization front. Organic carbon isotope results from rocks that have undergone various levels of decarbonization are relatively constant, with values similar to organic carbon in other Paleoproterozoic sedimentary rocks (−27.4±4.6‰: Strauss et al. 1992). This suggests that hydrothermal decarbonization went to chemical completion because a partial reaction would have fractionated the isotopes. The absence of gold in the calc-silicate pods, magnetite zones, dolerite sills, and lamprophyre dykes, all of which lacked graphite, confirms the necessity of graphite for gold deposition.

Table 2 Carbon isotope analyses of all 11 organic concentrates for which enough C was present for analysis

Drill hole	Depth (m)	Distance from ore	Position relative to ore	Unit	Rock type	Description	Whole-rock C (wt%)	$\delta^{34}C$ (‰ PDB)
DBD415	620.7	Distal	South limb; below	UBB	Calc-silicate replacement pod	Minor amphibole	0.21	−25.9
DBD415	624.0	Distal	South limb; below	UBB	Turbidite	Minor graphite, disseminated ilmenite	0.17	−24.2
DBD364	223.1	Intermediate	Above	UBB	Turbidite	Chlorite–biotite, moderate graphite	0.40	−23.6
DBD364	235.5	Intermediate	Above	UBB	Turbidite	Chlorite–biotite, moderate graphite	0.36	−22.8
DBD364	236.3	Intermediate	Above	UBB	Turbidite	Weak chlorite–biotite, moderate graphite	0.31	−22.4
DBD364	236.6	Intermediate	Above	UBB	Turbidite	Moderate graphite	0.48	−22.8
DBD364	331.7	Proximal	Above	UBB	Turbidite	Chlorite, minor graphite with decarbonization textures	0.12	−24.1
DBD395D5	974.6	Proximal	North limb; level	UBB	Turbidite	Minor graphite, disseminated ilmenite	0.12	−26.0
DBD364	343.6	Proximal	Above	CBC	Mudstone	Moderate graphite	0.57	−23.7
DBD395	1,080.1	Distal	North limb; below	MS	Mudstone	Graphite-rich	1.96	−23.9
DBD415	728.5	Intermediate	South limb; below	MS	Mudstone	Graphite-rich with partial decarbonization textures	1.15	−25.5

The samples are sorted first by stratigraphic unit, then by approximate distance to ore zones. The position of the sample relative to the ore zones is also noted; the south and north limbs refer to the DBS anticlinorium. The whole rock C content is from the original rock sample from which the organic concentrate was made.
UBB Upper Blake beds, *CBC* Callie boudin chert, *MS* Magpie schist

The reactions for the removal of graphite from the host rocks may be as simple as:

$$C_{(rock)} + O_{2\,(aq)} \rightarrow CO_{2\,(g)} \uparrow \quad (1)$$

$$C_{(rock)} + 2\,H_2O \rightarrow CO_{2\,(g)} \uparrow + 2\,H_{2\,(g)} \uparrow \quad (2)$$

or, given the negative correlation between $C/(C+CO_2)$ and $FeO/(FeO+Fe_2O_3)$ in the 57 decarbonized and graphitic samples (Fig. 9), may involve more complex reduction reactions as proposed by Thompson (1972):

$$\text{graphite} + 2\ \text{magnetite} + 2\ \text{K} - \text{feldspar} + 2\,H_2O_{(aq)} \rightarrow 2\ \text{biotite} + CO_{2\,(g)} \uparrow \quad (3)$$

$$13\ \text{graphite} + 26\ \text{magnetite} + 12\ \text{muscovite} + 24\ \text{quartz} + 36\,H_2O_{(aq)} \rightarrow 12\ \text{biotite} + 6\ \text{chlorite} + 13\ CO_{2(g)} \uparrow \quad (4)$$

In reactions 3 and 4, the oxygen required to liberate C is released from the reduction of the ferric iron component in magnetite to ferrous iron components in silicates, especially in biotite and chlorite. These reactions explain the absence of detrital or metamorphic magnetite and the scarcity of muscovite and feldspar in rocks around the ore zones because the reactions require relatively small amounts of graphite to consume large amounts of magnetite and K-silicate minerals. They are also consistent with the high Fe content of silicates, the high $FeO/(FeO+Fe_2O_3)$ ratios, and the low $C/(C+CO_2)$. The reactions could also proceed via

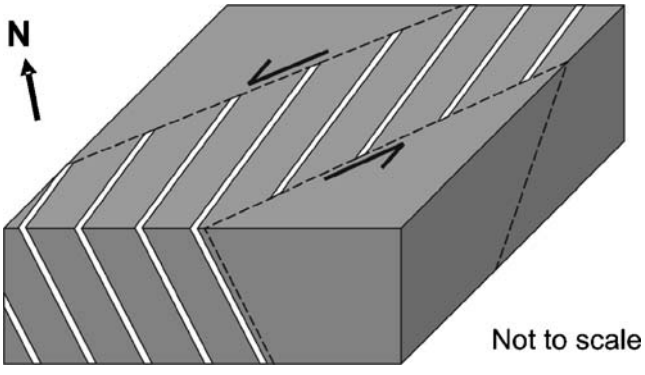

Fig. 13 Schematic diagram showing the proposed mechanism for the formation of ore-stage sheeted veins (*white*) at Callie within a sinistral semibrittle shear zone

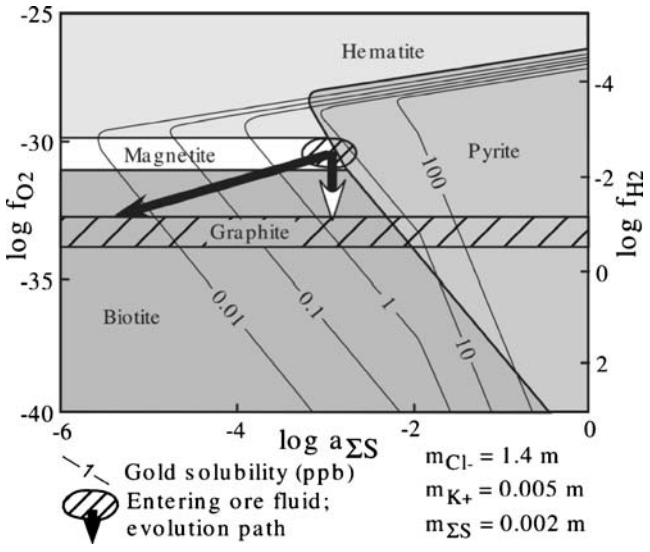

Fig. 14 A log f_{O2} versus log $a_{\Sigma S}$ diagram showing the possible evolution of ore fluids at Callie. The fluids were originally in equilibrium with magnetite (*hatched oval*) since the magnetite zones below the Callie deposit are unmodified. The *solid arrow* shows the evolution of the ore fluid in contact with graphitic rocks allowing for effervescence of CO_2, which would strongly partition H_2S into the gas phase destabilizing Au–bisulfide complexes and precipitating gold in the veins. The *open arrow* shows the evolution of the fluid without allowing for effervescence of CO_2; gold may still be precipitated as the fluid becomes more reduced, but the process is less effective than for effervescence of CO_2. This latter mechanism would result from oxidization of FeO in the wall rocks of the most Au-rich samples reducing the fluid and resulting in lower FeO/(FeO+Fe_2O_3). From Huston et al. (2006)

the reduction of ferric iron in preexisting silicates such as chlorite. All four reactions could occur simultaneously; reaction 1 would be more efficient in the presence of a relatively oxidized fluid, and the ferric iron and K-silicate content of the host rocks would limit reactions 3 and 4. As a result, reactions 1 and 2 may have been dominant in those decarbonized beds that do not show biotite augen development, due to an absence of ferric iron and K-silicate minerals, whereas those beds with more abundant ferric iron and K-silicate minerals may have developed the coarse biotite augen so commonly observed in and around the ore zones via reactions 3 and 4. An example of this is shown in Fig. 6g where an Au-rich sample contains no host rock biotite and <0.01 wt% C (lower quartile), with only 1.4 wt% Fe_2O_3 (second quartile), 9.3 wt% FeO (lower quartile), and 2.2 wt% K_2O (second quartile). The biotite augen growth during hydrothermal alteration is associated with a slight rotation of the augen relative to the dominant F_1/F_2 cleavage and therefore may reflect the dominant stress regime during the hydrothermal event—the same stress regime responsible for the QVC. The magnetite-rich zones below the deposit were not consumed by reactions 3 and 4 because there is no evidence that they ever contained graphite.

All of the above reactions would drive CO_2 effervescence as the CO_2 content of the ore fluid increases (Huston et al. 2006). This process is supported by the presence of CO_2-rich fluid inclusions (Mernagh and Wygralak, 2006, in review). Small quantities of CH_4, which was also present in the fluid inclusion data, would enhance effervescence due to the low solubility of CH_4 in hydrothermal fluids under mineralizing conditions (Naden and Shepherd 1989). Reaction of H_2, produced by reaction 2, with graphite could readily produce abundant CH_4. Effervescence would strongly partition H_2S out of the fluid and into the gas phase (Naden and Shepherd 1989), destabilizing Au–bisulfide complexes resulting in the precipitation of gold as shown by the solid arrow in Fig. 14 (Huston 1998; Huston et al. 2006). Loss of CO_2 via effervescence would also explain why carbonation is minor in the wall-rock alteration despite the large amounts of CO_2 that would have been produced by decarbonization and the CO_2-undersaturated nature of the rocks shown by extremely low CO_2/(Ca+Mg+Fe−S) values.

The close spatial association of gold with ilmenite, apatite, and xenotime is consistent with a linked genesis and indicates that the "immobile" elements Ti, Y, and P were mobile during gold deposition. Mobility of these elements has been recorded at other localities and has been explained by high CO_2 contents in the fluids (Hynes 1980; Van Baalen 1993) or high F (Gieré 1986; Van Baalen 1993). The elevated CO_2 content observed in fluid inclusions suggests that the fluids may have had high enough CO_2 concentrations to facilitate transport of Ti, Y, and P until CO_2 effervescence caused CO_2 loss from the fluid and deposition of these elements with gold. The presence of apatite may indicate that F was also abundant in the fluids.

In those rocks with the highest Au grades (>0.5 g/t), a slight decrease in FeO/(FeO+Fe_2O_3) ratios is evident (Table 1; Figs. 10a and 12). This indicates a slight oxidization of Fe^{2+} to Fe^{3+} in these most mineralized samples, consistent with a relatively oxidized fluid reacting with very reduced host rocks. The open arrow in Fig. 14 shows the fluid, originally in equilibrium with magnetite, becoming more reduced as it oxidizes the host rocks providing an additional, albeit less effective, mechanism for precipitating gold. This may have helped produce the higher Au grades in these samples and could have deposited Au where the reduced host rocks had previously been decarbonized or may never have had any organic carbon.

In detail, there is an inverse relationship between gold in the veins and sulfide minerals in the veins and adjacent wall rocks. Figure 12 shows that elevated sulfur abundances surround the QVC but sulfur is not abundant within it. This argues against wall-rock sulfidation as a possible mechanism for gold precipitation. This antithetic relationship also makes it difficult to establish timing relationships between the deposition of gold and the precipitation of sulfide

minerals. Although many of the sulfide minerals, especially arsenopyrite (Fig. 11c), may have been introduced during the hydrothermal event, the method for sulfide precipitation must have been different from that associated with gold precipitation. Effervescence of CO_2, which is the preferred mechanism for gold precipitation, should not precipitate sulfide minerals because H_2S would partition into the vapor phase and be lost from the fluid. Sulfide precipitation is interpreted to have occurred away from the gold-bearing veins as a consequence of fluid cooling (Huston 1998), by interaction with preexisting S in the host rocks, absence of veins to facilitate effervescence, or at lower fluid–rock ratios on the margins of the ore system. The zonation from proximal pyrrhotite to distal chalcopyrite in the barren veins may be consistent with cooling of the fluids away from the ore zones.

Conclusions

It is important to understand the mechanisms behind the formation of the Callie gold deposit because, although many other gold deposits are known in the area, Callie contains by far the largest single accumulation of gold. It formed as a result of the confluence of several factors beneficial for ore deposition: the preexisting DBS anticlinorium, which focused later fluid flow into anticlinal hinge zones; a transpressive structural regime, which allowed local extension to facilitate fluid flow and form the QVC; reactive reduced graphitic host units; and gold-bearing fluids. An effective exploration model would combine all of these. It is interesting to note that Callie contains two types of rocks which are common hosts for gold deposits in other areas of the Tanami Region, graphitic rocks, and iron formation-type rocks (the magnetite zones), but the most iron-rich rocks are barren at Callie.

The preexisting south–southeast plunging Callie anticlinorium focused fluid flow into the structure, and coincident east–southeast shear stresses under semibrittle conditions formed extensive sheeted quartz veining across the anticlinorium. Decarbonization of the graphitic, fine-grained, reduced, Fe-rich host rocks led to effervescence of CO_2 within the veins which would have been the primary mechanism for gold precipitation. Slight reduction of the fluid by the strongly reduced host rocks may have provided a secondary deposition mechanism for gold. Sulfide minerals, especially arsenopyrite, do not appear to be directly related to gold deposition but were introduced with the hydrothermal fluid and may be used a regional guide to hydrothermal fluid flow. Similarly, the magnetite-rich zones below the deposit appear to be unrelated to mineralization, but their resultant magnetic anomalies may be useful as indicators of areas of graphitic, Fe-rich reduced sediments.

Acknowledgments This study could not have taken place without the support and assistance of the Normandy NFM (now Newmont) staff at The Granites and DBS, especially John Campbell, James Emslie, Dave Larsen, Pip Sivwright, Kylie Haines, Tony Macolino, and the core shed staff. At Geoscience Australia, much help was received from members of the North Australia Craton Project; many thanks are especially due to David Huston, Terry Mernagh, and Geoff Fraser for their discussions, advice, and numerous reviews. Leon Vandenberg from the Northern Territory Geological Survey is thanked for the several extremely helpful discussions and clarifications of ideas. Phil Seccombe, Peter Neumayr, and Richard Goldfarb are thanked for their reviews which greatly improved the quality of the manuscript. John Pyke, Bill Pappas, Liz Webber, Algis Juodvalkis, and Graham Logan at Geoscience Australia are thanked for their help with analyses, as is Nick Ware at the Australian National University Research School of Earth Sciences. Shannon Parkinson drafted several of the figures. This paper is published with the permission of the CEO of Geoscience Australia.

References

Bagas L, Huston DL, Anderson J (2006) Gold deposits in the Palaeoproterozoic Tanami Group, Western Australia. Miner Depos (in press)

Bierlein FP, Fuller T, Stüwe K, Arne DC, Keays RR (1998) Wallrock alteration associated with turbidite-hosted gold deposits. Examples from the Palaeozoic Lachlan Fold Belt in central Victoria, Australia. Ore Geol Rev 13:345–380

Calvert SE, Pederson TF (1993) Geochemistry of recent oxic and anoxic marine sediments: implications for the geological record. Mar Geol 113:67–88

Cann JR (1970) Rb, Sr, Y, Zr and Nb in some ocean floor basaltic rocks. Earth Planet Sci Lett 10:7–11

Cooper JA, Ding PQ (1997) Zircon ages constrain the timing of deformation events in The Granites–Tanami Region, northwest Australia. Aust J Earth Sci 44:777–787

Crispe AJ, Scrimgeour IR, Vandenberg LC (2006) Geological framework of the Palaeoproterozoic Tanami Region, Northern Territory. Miner Depos (in press)

Cross AJ, Crispe AJ (2006) SHRIMP U–Pb analyses of detrital zircon: a window to understanding the early Paleoproterozoic development of the Tanami basin, northern Australia. Miner Depos (in press)

Cross AJ, Fletcher IF, Crispe AJ, Huston DL, Williams N (2005) New constraints on the timing of deposition and mineralisation in the Tanami Group. North Territ Geol Surv Rec 1:44–45

Davis GH, Reynolds SJ (1996) Shear zones and progressive deformation. In: Structural geology of rocks and regions, 2nd edn. Wiley, New York, pp 493–563

Dean AA (2001) Igneous rocks of the Tanami Region. North Territ Geol Surv Rec 3:78

Deer WA, Howie RA, Zussman J (1992) An introduction to the rock-forming minerals, 2nd edn. Longman, England, p 696

Eilu P, Groves DI, Mikucki EJ, McNaughton NJ, Ridley JR (1995) Alteration indices and pathfinder elements in wallrock alteration zones around Archaean lode-gold deposits. In: Pasava J, Kribek B, Zak K (eds) Mineral deposits: from their origin to their environmental impacts. Balkema, Rotterdam, pp 113–116

Eilu P, Mikucki EJ, Groves DI (1997) Wallrock alteration and primary geochemical dispersion in lode-gold exploration. SGA Short Course Ser 1:65

Ferry JM (1992) Regional metamorphism of the Waits River Formation, eastern Vermont: delineation of a new type of giant metamorphic hydrothermal system. J Petrol 33:45–94

Fraser G (2002) Timing of regional tectonism and Au-mineralisation in the Tanami Region: $^{40}Ar/^{39}Ar$ geochronological constraints: North Territ Geol Surv Rec 3. Accessible online at http://www.ga.gov.au/pdf/RR0051.pdf

Frost (1991) Stability of oxide minerals in metamorphic rocks. In: Lindsley DH (ed) Oxide minerals: petrologic and magnetic significance. Rev Miner 25:470–487

Gieré R (1986) Zirconolite, allanite and hoegbomite in a marble skarn from the Bergell contact aureole; implications for mobility of Ti, Zr and REE. Contrib Miner Petrol 93:459–470

Haines K (1999) An investigation of the contact and alteration of the Callie Host Unit and Magpie Schist Unit, Callie gold deposit, Northern Territory, Australia. University of Adelaide Honours thesis, University of Adelaide, Adelaide

Hendrickx MA, Slater K, Crispe AJ, Dean AA, Vandenberg LC, Smith J (2000) Paleoproterozoic stratigraphy of the Tanami Region: regional correlations and relation to mineralization-preliminary results. North Territ Geol Surv Rec GS 13:66

Huston DL (1998) The hydrothermal environment. AGSO J Aust Geol Geophys 17:15–30

Huston DL, Wygralak A, Mernagh T, Vandenberg L, Crispe A, Lambeck L, Bagas L, Cross A, Fraser G, Williams N, Worden K, Meixner T (2006) Lode gold mineral system(s) of the Tanami Region, northern Australia. Miner Depos (in press)

Hynes A (1980) Carbonatization and mobility of Ti, Y, and Zr in Ascot Formation metabasalts, SE Quebec. Contrib Miner Petrol 75:79–87

Jenner GA, Longerich HP, Jackson SE, Fryer BJ (1990) ICP-MS: a powerful tool for high-precision trace-element analysis in earth sciences: evidence from analysis of selected USGS reference samples. Chem Geol 83:133–148

Jones B, Manning DAC (1994) Comparison of geochemical indices used for the interpretation of paleoredox conditions in ancient mudstones. Chem Geol 111:111–129

Kimura H, Watanabe Y (2001) Ocean anoxia at the Precambrian–Cambrian boundary. Geology 29:995–998

Lewan MD (1984) Factors controlling the proportionality of vanadium to nickel in crude oils. Geochim Cosmochim Acta 48:2231–2238

Lovering TG, Hedal JA (1987) Trace elements in magnetic concentrates from stream sediments in southwestern New Mexico—a potential tool for reconnaissance geochemical exploration in arid lands. US Geol Surv Bull 1566:31

Mason B (1982) Principles of geochemistry. Wiley, New York, p 329

Mayer TE (1990) The Granites gold field. In: Hughes FE (ed) Geology of the mineral deposits of Australia and Papua New Guinea. The Australasian Institute of Mining and Metallurgy, Melbourne, pp 719–724

Morand VJ (1994) Calc-silicate lenses in the Early Palaeozoic mud-pile of the Lachlan Fold Belt. Aust J Earth Sci 41:383–386

Naden J, Shepherd TJ (1989) Role of methane and carbon dioxide in gold deposition. Nature 342:793–795

Nesbitt HW, Young GM (1989) Formation and diagenesis of weathering profiles. J Geol 97:129–147

Norrish K, Chappell BW (1977) X-ray fluorescence spectrometry. In: Zussman J (ed) Physical methods in determinative mineralogy. Academic, London, pp 201–272

Pyke J (2000) Minerals laboratory staff develops new ICP-Magpie Schist preparation method. AGSO Geosci Aust Res Newsl 33:12–14

Radzik NA (1998) The relationship between magnetite occurrence and gold mineralization in the Callie gold deposit, Tanami Region, Northern Territory, Australia. University of Adelaide Honours thesis, University of Adelaide, Adelaide

Robl TL, Davis BH (1993) Comparison of the HF-HCl and HF-BF_3 maceration techniques and the chemistry of resultant organic concentrates. Org Geochem 20:249–255

Rumble D (1976) Oxide minerals in metamorphic rocks. In: Rumble D (ed) Oxide minerals: Rev Miner 3:R1–R24

Shapiro L, Brannock WW (1962) Rapid analysis of silicate, carbonate, and phosphate rocks. US Geol Surv Bull B 1144-A:A1–A56

Smith ME, Lovett DR, Pring PI, Sando BG (1998) Dead Bullock Soak gold deposits. In: Berkman DA, Mackenzie DH (eds) Geology of Australian and Papua New Guinean mineral deposits. The Australasian Institute of Mining and Metallurgy, Melbourne, pp 449–460

Strauss H, Des Marais DJ, Hayes JM, Summons RE (1992) The carbon-isotopic record. In: Schopf JW, Klein C (eds) The Proterozoic biosphere. Cambridge University Press, New York, pp 117–128

Taylor SR, McLennan SM (1985) The continental crust: its composition and evolution. Blackwell, Melbourne, p 312

Thompson JB Jr (1972) Oxides and sulfides in regional metamorphism of pelitic schists. Proc Int Geol Congr 10:27–35

Tunks A, Marsh S (1998) Gold deposits of the Tanami Corridor. In: Berkman DA, Mackenzie DH (eds) Geology of Australian and Papua New Guinean mineral deposits. The Australasian Institute of Mining and Metallurgy, Melbourne, pp 443–448

Van Baalen MR (1993) Titanium mobility in metamorphic systems: a review. Chem Geol 110:233–249

Vandenberg LC, Hendrickx MA, Crispe AJ (2001) Structural geology of the Tanami Region. North Territ Geol Surv Rec 4:28

Voulgaris P, Emslie J (2004) Geology and ore estimation at the Callie underground gold mine, Tanami, NT. Australasian Inst Min Metall Bull 2:71–78

Wedepohl KH (1995) The composition of the continental crust. Geochim et Cosmochim Acta 59:1217–1232

Wygralak AS, Mernagh TP, Fraser G, Huston DL, Denton G, McInnes B, Crispe A, Vandenberg LC (2001) Gold mineral systems in the Tanami Region. AGSO Res Newsl 34:2–14

Wygralak AS, Mernagh TP, Huston DL, Ahmad M (2004) Gold mineral system of the Tanami Region. North Territ Geol Surv Rep 18, p 90